

Variational quantum algorithm for anion exchange across electrolyzer membrane

Timur Gubaev,¹ Philipp Pfeffer,¹ Christian Dreßler,² and Jörg Schumacher¹

¹*Institute of Thermodynamics and Fluid Mechanics,*

Technische Universität Ilmenau, P.O. Box 100565, D-98684 Ilmenau, Germany

²*Institute of Physics, Technische Universität Ilmenau, P.O. Box 100565, D-98684 Ilmenau, Germany*

(Dated: December 2, 2025)

We present a variational quantum algorithm that solves the one-dimensional diffusion problem with a space-dependent diffusion constant $D(x)$. This problem is relevant for the exchange of hydroxide ions across a multi-layer membrane in an alkaline electrolyzer. We use 16 to 64 grid points across the membrane, resulting from $n = 4$ to 6 data qubits for the ideal quantum simulations that are based on the Qiskit software. For these qubit numbers, the depth of the parametric quantum circuit has been chosen to ensure sufficient expressibility. The state preparation requires particular attention since the diffusivity D is piecewise constant in the different layers with discontinuities at the interface. Furthermore, we compare different classical optimization schemes with respect to their convergence in the VQA method. We demonstrate the applicability of the quantum algorithm to a problem with non-trivial boundary conditions and jump conditions of the diffusion constant and outline possible extensions of the proof-of-concept application case of quantum computing.

I. INTRODUCTION

Electrolyzers and fuel cells are a central component for enabling the transformation to a green economy, which use electricity, e.g. from renewable energy, to split water into oxygen and hydrogen — a clean fuel and carrier of energy [1, 2]. Membranes and diaphragms are key components of alkaline electrolyzers, where they separate the anode and cathode compartments while allowing ionic transport. Conventional alkaline water electrolysis (AWE) employs porous diaphragms such as Zirfon (ZrO₂-polysulfone), valued for their mechanical stability, chemical durability, and low area resistance ($\sim 0.1 \Omega \text{ cm}^2$ at 80 °C in 30 wt% KOH) [3]. However, their relatively high gas crossover, especially under pressure gradients between cathode and anode, limits efficiency and safety in pressurized operation [4, 5]. In contrast, anion exchange membranes (AEMs) offer low H₂/O₂ crossover and enable differential pressure operation [6, 7], but suffer from limited mechanical robustness and higher cost. Recent reviews highlight the potential of hybrid or graded separators that combine the dense, selective character of AEMs with the mechanical stability of porous supports (multi-layered AEM) [8, 9]. Such configurations will be studied in the following.

The transport of the negatively charged anions across the membrane is macroscopically modeled as a diffusion process with a space-dependent diffusion constant, see e.g. [10]. The numerical modeling of these transport processes is established by a broad spectrum of methods ranging from microscopic molecular dynamics models [11–13] to one- and two-dimensional diffusion processes with or without additional drift terms, which are for example caused by electrical fields [14].

The solution of classical physics problems using quantum computing [15, 16] is an emerging research field, which explores the potential capabilities of quantum devices and systems to study dynamics that is often formulated in the form of partial differential equations (PDE),

such as in fluid mechanics [17–19]. One class of algorithms to investigate transport processes are variational quantum algorithms (VQA). When applied to solving differential equations, VQAs typically reformulate the problem as an optimization task; they are hybrid quantum-classical algorithms [20]. A popular field of application are linear one-dimensional advection-diffusion equations for simple transport problems [21–26]. The framework was extended from frequently used periodic [25] to Dirichlet and Neumann boundary conditions in ref. [27]. Furthermore, linear heat equations in one and two dimensions were considered by VQAs in refs. [28, 29]. VQA applications to nonlinear partial differential equations include steady [30] and time-dependent [31] one-dimensional nonlinear Schrödinger equations, as well as the one-dimensional Burgers equation [30, 32, 33]. In refs. [32, 33] an alternative Feynman-Kitaev algorithm is used which orders spatial and temporal qubits in one register and thus avoids time stepping.

In the present work, we investigate the diffusive anion transport problem across a multi-layered AEM by a variational quantum algorithm in an ideal quantum simulation framework. The studied classical field is the anion concentration $c(x, t)$ for $t > 0$ and $x \in [\tilde{x}_0, \tilde{x}_m]$. In contrast to a recent quantum spectral method for constant diffusion [34], our application is characterized by a linear PDE with piecewise constant diffusion constants $D(x)$ in the different layers of the AEM,

$$\frac{\partial c}{\partial t} = \mathcal{L}[c(x, t), D(x)] = \frac{\partial}{\partial x} \left(D(x) \frac{\partial c}{\partial x} \right), \quad (1)$$

where \mathcal{L} is a linear operator. We apply different Dirichlet boundary conditions at the two ends of the membrane cross-section, which have to be included in the variational formulation. We derive an analytical solution for the temporal relaxation to a steady ion concentration, which allows us to validate the quantum algorithm for different grid resolutions, which are connected to the number of qubits: a discretization of the interval into N equidistant

mesh cells requires $n = \log_2(N)$ qubits. The state preparation is adapted here to capture for the discontinuities of D in the multi-layered AEM. In addition, we compare different optimization algorithms for the problem at hand, among them a recently suggested surrogate model-based optimization scheme [35] for the search of the minimum of nonconvex cost functions. This optimization step of the VQA typically complicates complexity estimates of the algorithm as the optimization procedure can run into barren plateaus [36]. Furthermore, we investigate the expressivity of the quantum ansatz for different depths [37]. Our proof-of-concept study demonstrates the capability of VQA algorithms to solve the concrete application case at hand. We discuss possible straight extensions of the anion transport problem.

The hybrid quantum-classical nature of VQAs implies that the cost function $C(\boldsymbol{\lambda})$ is minimized classically by an optimization method [20]. This cost function is evaluated by a parametric quantum circuit, which is composed of n qubits and single- and two-qubit gates. The cost minimum search is performed classically in a high-dimensional parameter space of dimension $M \sim \mathcal{O}(N)$ that contains a parameter vector $\boldsymbol{\lambda}$. This parameter vector $\boldsymbol{\lambda}$, which consists of the angles of the single-qubit unitary rotation gates $\boldsymbol{\lambda} = (\lambda_1, \lambda_2, \dots, \lambda_M) \in \mathbb{R}^M$, is the input to the algorithm. Several approaches exist for the implementation, such as minimizing the Euclidean distance between the VQA and a finite difference solution [25], or adopting a weak variational formulation [27], the latter of which will be used here (and detailed below).

The outline is as follows. In Sec. II, we explain the classical framework including the analytical solution of the initial-boundary value problem, the relaxation rate to the steady state profile, and the finite difference method which will be used for the comparison with the quantum algorithm. Section III discusses the specifics of the variational quantum algorithm including the quantum state preparation. In Sec. IV, the results and analyses are presented. This includes expressibility study, a comparison of classical optimization algorithms, and a detailed discussion of the time evolution towards the steady solution in comparison to the classical finite difference method. We conclude with a summary and an outlook.

II. CLASSICAL FRAMEWORK

A. Problem description and analytical solution

We employ a variational quantum algorithm (VQA) to numerically simulate hydroxide-ion transport in alkaline water electrolysis. This diffusive transport process with spatially varying diffusivity D is depicted in Fig. 1(a). The system produces hydrogen gas at the cathode by reducing water molecules, generating hydroxide ions as a byproduct. These hydroxide ions migrate through the anion exchange membrane (AEM) to the anode, where they are oxidized to produce oxygen gas and release elec-

trons. The process efficiently converts electrical energy to chemical energy stored in hydrogen, while safely separating hydrogen and oxygen production. The number of layers in the original AEM electrolysis problem can be reduced to two layers, see Fig. 1(b), by assuming that the electrolytes are well-mixed, such that the charge distribution within them remains uniform.

The anion-exchange membrane electrolysis problem is described by the one-dimensional diffusion equation (1) with piecewise-constant diffusivity in $\Omega_T = (\tilde{x}_0, \tilde{x}_m) \times (0, T]$. The following initial condition,

$$c(x, 0) = c_0(x), \quad (2)$$

and Dirichlet boundary conditions do hold,

$$c(\tilde{x}_0, t) = c_{0,1} \quad \text{and} \quad c(\tilde{x}_m, t) = c_{0,m}, \quad (3)$$

where $\tilde{x}_0 = 0\ell$ and $\tilde{x}_m = 1\ell$, are boundaries, ℓ is the characteristic length unit of sub-millimeter size, m is the number of layers, T is the time horizon, $c_0(x)$ is the initial condition at location x , $c_{0,1}$ is the concentration at the left boundary and $c_{0,m}$ is the concentration at the right boundary. While \tilde{x}_0 and \tilde{x}_m are the boundary points, locations $\tilde{x}_1, \tilde{x}_2, \dots, \tilde{x}_{m-1}$ represent the interfaces between the layers. For example, the number of layers is $m = 4$ for the problem in Fig. 1(a) with interfaces \tilde{x}_1 , \tilde{x}_2 and \tilde{x}_3 and $m = 2$ for the problem in Fig. 1(b) with a single interface \tilde{x}_1 , respectively. Interfaces are subject to interface conditions discussed in the next section.

In eqns. (1) and (2), the diffusion coefficient $D(x)$ and the initial conditions $c_0(x)$ are piecewise-constant functions defined as

$$D(x) = D_j, \quad (4)$$

$$c_0(x) = c_{0,j}, \quad (5)$$

for $\tilde{x}_{j-1} \leq x < \tilde{x}_j$ and $j = 1, \dots, m$. Throughout this work, diffusion constants $D_j \sim 10^{-8} \text{ m}^2/\text{s}$ are expressed in characteristic units of ℓ^2/τ_D , where $\tau_D = \ell^2/D_1$ defines the characteristic time unit. Note that at the interface positions \tilde{x}_j the diffusion coefficient and the initial concentration is taken from the region to the right of the interface. In the following sections the steady-state and analytical solutions will be derived for an arbitrary number of layers m .

1. Steady-state analytical solution

To obtain the steady-state solution in the presence of discontinuities, the right-hand side of (1) is equated to zero in m individual regions $(\tilde{x}_{j-1}, \tilde{x}_j)$ with each region corresponding to the j -th layer, and, additionally, interface conditions are imposed at the interfaces $\tilde{x}_1, \tilde{x}_2, \dots, \tilde{x}_{m-1}$ between the layers where discontinuities arise. When a region $(\tilde{x}_{j-1}, \tilde{x}_j)$ is considered, the equation (1) simplifies as,

$$\frac{\partial c}{\partial t} = \frac{\partial}{\partial x} \left(D(x) \frac{\partial c}{\partial x} \right) \Rightarrow \frac{\partial c}{\partial t} = D_j \frac{\partial^2 c}{\partial x^2},$$

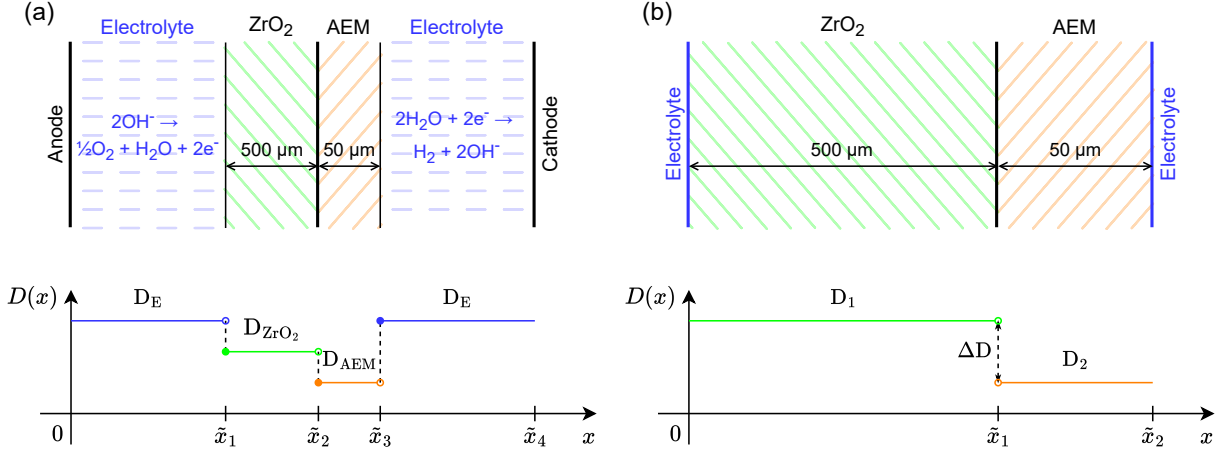


FIG. 1: Sketch of the anion-exchange membrane (AEM). (a) The 4-layer AEM electrolysis system. (b) The simplified configuration, which will be used for the actual quantum computation approximates the two electrolyte reservoirs by Dirichlet conditions for the anion concentration at the corresponding outer membrane interfaces. The layer ZrO_2 refers to Zirfon, a composite material consisting of ZrO_2 embedded in a polysulfone matrix.

where D_j is the diffusivity of the j -th layer. Then, the right-hand side of the simplified equation is equated to zero while treating $c(x, t)$ as the steady-state solution $c_s(x)$, and an integral is taken with respect to x ,

$$D_j \frac{\partial^2 c_s}{\partial x^2} = 0 \quad \Rightarrow \quad D_j \frac{dc_s}{dx} = J_j,$$

where J_j is the flux in the j -th layer. Taking another integral yields the steady-state solution for $\tilde{x}_{j-1} \leq x < \tilde{x}_j$ and $j = 1, \dots, m$,

$$c_s(x) = \frac{J_j}{D_j} x + b_j,$$

where b_j is an integration constant. Next, to further address the discontinuities and determine the unknowns J_j and b_j , the interface conditions are imposed at the interface positions \tilde{x}_j as $j = 1, 2, \dots, m-1$ along with boundary conditions, namely

$$\lim_{x \rightarrow \tilde{x}_j^-} c_s(x) = \lim_{x \rightarrow \tilde{x}_j^+} c_s(x), \quad (6)$$

$$\lim_{x \rightarrow \tilde{x}_j^-} D(x) \frac{dc_s}{dx} = \lim_{x \rightarrow \tilde{x}_j^+} D(x) \frac{dc_s}{dx}, \quad (7)$$

$$c_s(\tilde{x}_0) = c_{0,1} \quad \text{and} \quad c_s(\tilde{x}_m) = c_{0,m}. \quad (8)$$

Equations (6) and (7) correspond to solution and flux continuity, respectively, at interface positions. Eq. (7) is satisfied when $J_j = J_{j+1}$, meaning that fluxes in all m layers are equal and can be equated to a global flux J , thus leaving only m unknown constants b_j and one unknown flux J ,

$$J_1 = J_2 = \dots = J_m = J.$$

Substituting for c_s in eqns. (6) and (8), and using the global flux J results in the following linear system:

$$\frac{J}{D_j} \tilde{x}_j + b_j = \frac{J}{D_{j+1}} \tilde{x}_j + b_{j+1}, \quad (9)$$

$$\frac{J}{D_1} \tilde{x}_0 + b_1 = c_{0,1}, \quad (10)$$

$$\frac{J}{D_m} \tilde{x}_m + b_m = c_{0,m}. \quad (11)$$

Equations (9) and (10) can be rewritten as a recurrence relation of b_j in terms of J as:

$$b_1 = c_{0,1} - \frac{J}{D_1} \tilde{x}_0, \quad (12)$$

$$b_j = b_{j-1} + J (D_{j-1}^{-1} - D_j^{-1}) \tilde{x}_{j-1}, \quad (13)$$

for $j = 2, 3, \dots, m$. Unrolling eqns. (12) and (13) produces a non-recursive closed-form formula for arbitrary b_j in terms of the flux J :

$$b_j = J \left[\sum_{k=2}^j [(D_{k-1}^{-1} - D_k^{-1}) \tilde{x}_{k-1}] - D_1^{-1} \tilde{x}_0 \right] + c_{0,1} \quad (14)$$

Using (14) to evaluate b_m and combining it with (11) produces an expression for J which is given by

$$J = \frac{c_{0,m} - c_{0,1}}{D_m^{-1} \tilde{x}_m + \sum_{k=2}^m [(D_{k-1}^{-1} - D_k^{-1}) \tilde{x}_{k-1}] - D_1^{-1} \tilde{x}_0}. \quad (15)$$

To simplify the expression for c_s and further derivations, the prefactor of x in $c_s(x)$ is defined as:

$$a_j = \frac{J}{D_j}. \quad (16)$$

The steady-state solution is then expressed as

$$c_s(x) = a_j x + b_j, \quad \tilde{x}_{j-1} \leq x < \tilde{x}_j, \quad j = 1, \dots, m. \quad (17)$$

To calculate the steady-state solution the flux J is obtained first using (15). Then a_j are computed using (16), and b_j are computed using recurrence relation (12) and (13).

2. Full time-dependent analytical solution

Similarly to the heat equation with uniform thermal diffusivity, eq.(1) is solved by the method of separation of variables. We use the ansatz

$$c(x, t) = K(x)T(t). \quad (18)$$

In each region $(\tilde{x}_{j-1}, \tilde{x}_j)$, (1) simplifies as:

$$\frac{\partial c}{\partial t} = D_j \frac{\partial^2 c}{\partial x^2} \quad \text{in} \quad \Omega_T = (\tilde{x}_{i-1}, \tilde{x}_i) \times (0, T]. \quad (19)$$

Substituting (18) into (19) and rearranging terms gives

$$\frac{1}{T(t)} \frac{dT}{dt} = \frac{D_j}{K_j(x)} \frac{d^2 K_j}{dx^2}. \quad (20)$$

Since left-hand and right-hand sides of (20) have to be equal for all x and t , they must be equal to some separation constant which can be written as $-\lambda_k^2$. This gives rise to two ordinary differential equations for each λ_k^2 :

$$\frac{dT_k}{dt} + \lambda_k^2 T_k(t) = 0, \quad (21)$$

$$\frac{d^2 K_{jk}}{dx^2} + \frac{\lambda_k^2}{D_j} K_{jk}(x) = 0. \quad (22)$$

The solution to (21) reads $T_k(t) = C_k \exp(-\lambda_k^2 t)$. However, since $c(x, t) = K(x)T(t)$ the constant C_k can be absorbed by the constants appearing in the solution of (22). Therefore, (21) and (22) admit the following solutions:

$$T_k(t) = \exp(-\lambda_k^2 t), \quad (23)$$

$$K_{jk}(x) = \tilde{A}_{jk} \exp\left(-i \frac{\lambda_k}{\sqrt{D_j}} x\right) + \tilde{B}_{jk} \exp\left(i \frac{\lambda_k}{\sqrt{D_j}} x\right). \quad (24)$$

To simplify the further derivation, the following substitutions for constants A_{jk} and B_{jk} are introduced such

that:

$$\tilde{A}_{jk} = \frac{1}{2} \left[A_{jk} \exp\left(i \frac{\lambda_k}{\sqrt{D_j}} \tilde{x}_{j-1}\right) + i B_{jk} \exp\left(i \frac{\lambda_k}{\sqrt{D_j}} \tilde{x}_{j-1}\right) \right], \quad (25)$$

$$\tilde{B}_{jk} = \frac{1}{2} \left[A_{jk} \exp\left(-i \frac{\lambda_k}{\sqrt{D_j}} \tilde{x}_{j-1}\right) - i B_{jk} \exp\left(-i \frac{\lambda_k}{\sqrt{D_j}} \tilde{x}_{j-1}\right) \right]. \quad (26)$$

Substituting eqns. (25) and (26) into eq. (24) yields the following expression in terms of the newly introduced coefficients A_{jk} and B_{jk} :

$$K_{jk}(x) = A_{jk} \cos\left(\frac{\lambda_k}{\sqrt{D_j}}(x - \tilde{x}_{j-1})\right) + B_{jk} \sin\left(\frac{\lambda_k}{\sqrt{D_j}}(x - \tilde{x}_{j-1})\right). \quad (27)$$

The solution $c(x, t)$ is subject to boundary, continuity and flux continuity conditions at interfaces x_i as $i = 1, 2, \dots, m-1$. This implies the following conditions,

$$\lim_{x \rightarrow \tilde{x}_i^-} c(x, t) = \lim_{x \rightarrow \tilde{x}_i^+} c(x, t), \quad (28)$$

$$\lim_{x \rightarrow \tilde{x}_i^-} D(x) \frac{\partial c}{\partial x} = \lim_{x \rightarrow \tilde{x}_i^+} D(x) \frac{\partial c}{\partial x}, \quad (29)$$

$$c(\tilde{x}_0, t) = 0 \quad \text{and} \quad c(\tilde{x}_m, t) = 0. \quad (30)$$

Substituting $K_j(x)$ and $T(x)$ into these equations yields,

$$A_{1k} = 0, \quad (31)$$

$$A_{j+1,k} = A_{jk} \cos\left(\frac{\lambda_k(\tilde{x}_j - \tilde{x}_{j-1})}{\sqrt{D_j}}\right) + B_{jk} \sin\left(\frac{\lambda_k(\tilde{x}_j - \tilde{x}_{j-1})}{\sqrt{D_j}}\right) \quad (32)$$

$$\frac{\sqrt{D_{j+1}}}{\sqrt{D_j}} B_{j+1,k} = -A_{jk} \sin\left(\frac{\lambda_k(\tilde{x}_j - \tilde{x}_{j-1})}{\sqrt{D_j}}\right) + B_{jk} \cos\left(\frac{\lambda_k(\tilde{x}_j - \tilde{x}_{j-1})}{\sqrt{D_j}}\right), \quad (33)$$

and

$$A_{mk} \cos\left(\frac{\lambda_k(\tilde{x}_m - \tilde{x}_{m-1})}{\sqrt{D_m}}\right) + B_{mk} \sin\left(\frac{\lambda_k(\tilde{x}_m - \tilde{x}_{m-1})}{\sqrt{D_m}}\right) = 0. \quad (34)$$

One can see that eqns. (31), (32), and (33) represent a recurrence relation. One starts with $A_{1k} = 0$ and an unknown B_{1k} to calculate A_{jk} and B_{jk} for $j = 2, 3, \dots, m$.

These equations together with (34) can be converted into a form that is independent of B_{1k} . To this end, we introduce reduced coefficients \hat{A}_{jk} and \hat{B}_{jk} and a corresponding reduced spatial solution $\hat{K}_{jk}(x)$, such that

$$A_{jk} = B_{1k} \hat{A}_{jk} \quad \text{and} \quad B_{jk} = B_{1k} \hat{B}_{jk}. \quad (35)$$

Furthermore,

$$\begin{aligned} \hat{K}_{jk}(x) = & \hat{A}_{jk} \cos \left(\frac{\lambda_k}{\sqrt{D_j}} (x - \tilde{x}_{j-1}) \right) \\ & + \hat{B}_{jk} \sin \left(\frac{\lambda_k}{\sqrt{D_j}} (x - \tilde{x}_{j-1}) \right). \end{aligned} \quad (36)$$

Notice that spatial solutions $K_{jk}(x)$ are now expressed in terms of unknown coefficients B_{1k} and reduced spatial solutions $\hat{K}_{jk}(x)$, i.e.,

$$K_{jk}(x) = B_{1k} \hat{K}_{jk}(x). \quad (37)$$

This leads to a new set of equations

$$\hat{A}_{1k} = 0 \quad \text{and} \quad \hat{B}_{1k} = 1, \quad (38)$$

$$\begin{aligned} \hat{A}_{jk} = & \hat{A}_{j-1,k} \cos \left(\frac{\lambda_k (\tilde{x}_{j-1} - \tilde{x}_{j-2})}{\sqrt{D_{j-1}}} \right) \\ & + \hat{B}_{j-1,k} \sin \left(\frac{\lambda_k (\tilde{x}_{j-1} - \tilde{x}_{j-2})}{\sqrt{D_{j-1}}} \right), \end{aligned} \quad (39)$$

$$\begin{aligned} \hat{B}_{jk} = & -\sqrt{\frac{D_{j-1}}{D_j}} \hat{A}_{j-1,k} \sin \left(\frac{\lambda_k (\tilde{x}_{j-1} - \tilde{x}_{j-2})}{\sqrt{D_{j-1}}} \right) \\ & + \sqrt{\frac{D_{j-1}}{D_j}} \hat{B}_{j-1,k} \cos \left(\frac{\lambda_k (\tilde{x}_{j-1} - \tilde{x}_{j-2})}{\sqrt{D_{j-1}}} \right), \end{aligned} \quad (40)$$

$$\begin{aligned} 0 = & \hat{A}_{mk} \cos \left(\frac{\lambda_k (\tilde{x}_m - \tilde{x}_{m-1})}{\sqrt{D_m}} \right) \\ & + \hat{B}_{mk} \sin \left(\frac{\lambda_k (\tilde{x}_m - \tilde{x}_{m-1})}{\sqrt{D_m}} \right). \end{aligned} \quad (41)$$

The recurrence relations governed by equations (38), (39) and (40) together with (41) represent a non-linear recursive equation in terms of λ_k . It is solved numerically using, e.g., a bracketing algorithm, since all roots of this equation are at zero-crossings. This results in multiple separation constants λ_k .

After solving the non-linear recursive equation above for λ_k , equations (38), (39), (40) are reused to calculate the reduced coefficients \hat{A}_{jk} and \hat{B}_{jk} and the reduced spatial solutions $\hat{K}_{jk}(x)$. Then, according to (37) the spatial solutions $K_{jk}(x)$ can be written down in terms of the reduced spatial solutions $\hat{K}_{jk}(x)$ and the coefficients B_{1k} which are essentially the expansion coefficients of the infinite series representing the solution to the original problem. To obtain the expansion coefficients B_{1k} , the following integration is carried out:

$$B_{1k} = \frac{1}{G_k} \sum_{j=1}^m \int_{\tilde{x}_{j-1}}^{\tilde{x}_j} (c_0(x) - c_s(x)) \hat{K}_{jk}(x) dx,$$

which results in

$$\begin{aligned} B_{1k} = & \frac{1}{G_k} \sum_{j=1}^m \frac{D_j}{\lambda_k^2} \left[a_j \hat{A}_{jk} + \frac{\lambda_k}{\sqrt{D_j}} (c_{0j} - c_s(\tilde{x}_{j-1})) \right. \\ & - \left(a_j \hat{A}_{jk} + \frac{\lambda_k}{\sqrt{D_j}} (c_{0j} - c_s(\tilde{x}_j)) \right) \\ & \times \hat{B}_{jk} \cos \left(\frac{\lambda_k}{\sqrt{D_j}} (\tilde{x}_j - \tilde{x}_{j-1}) \right) \\ & + \left(-a_j \hat{B}_{jk} + \frac{\lambda_k}{\sqrt{D_j}} (c_{0j} - c_s(\tilde{x}_j)) \right) \\ & \times \hat{A}_{jk} \sin \left(\frac{\lambda_k}{\sqrt{D_j}} (\tilde{x}_j - \tilde{x}_{j-1}) \right) \left. \right], \end{aligned} \quad (42)$$

where G_k are normalization constants. The normalization constants are found by the following integration:

$$G_k = \sum_{j=1}^m \int_{\tilde{x}_{j-1}}^{\tilde{x}_j} \hat{K}_{jk}^2(x) dx$$

which yields:

$$\begin{aligned} G_k = & \sum_{j=1}^m \frac{\sqrt{D_j}}{4\lambda_k} \left[2\hat{A}_{jk} \hat{B}_{jk} \right. \\ & + 2 \frac{\lambda_k}{\sqrt{D_j}} (\tilde{x}_j - \tilde{x}_{j-1}) (\hat{A}_{jk}^2 + \hat{B}_{jk}^2) \\ & - 2\hat{A}_{jk} \hat{B}_{jk} \cos \left(2 \frac{\lambda_k}{\sqrt{D_j}} (\tilde{x}_j - \tilde{x}_{j-1}) \right) \\ & \left. + (\hat{A}_{jk}^2 - \hat{B}_{jk}^2) \sin \left(2 \frac{\lambda_k}{\sqrt{D_j}} (\tilde{x}_j - \tilde{x}_{j-1}) \right) \right]. \end{aligned}$$

To compute the analytical solution one first solves the non-linear recursive equation governed by (38), (39), (40) and (41) to obtain the separation constants λ_k . Then the obtained λ_k are used to compute the reduced coefficients \hat{A}_{jk} and \hat{B}_{jk} using the recurrence relation (38), (39), and (40). Subsequently, the reduced spatial solutions $\hat{K}_{jk}(x)$ are computed as well. Next, the normalization constants G_k are computed. The expansion coefficients B_{1k} are computed afterwards and combined with \hat{A}_{jk} and \hat{B}_{jk} using (35) to produce the coefficients A_{jk} and B_{jk} . Finally, the piecewise solution is written as

$$c(x, t) = c_s(x) + \sum_{k=1}^{\infty} \exp(-\lambda_k^2 t) K_{jk}(x), \quad (43)$$

for $\tilde{x}_{j-1} \leq x < \tilde{x}_j$. The graph of the analytical solution (43) is shown in Fig. 2. A system consisting of 4 layers with diffusion coefficients $D_1 = D_4 = 1 \ell^2/\tau_D$, $D_2 = 0.75 \ell^2/\tau_D$, and $D_3 = 0.5 \ell^2/\tau_D$ and initial conditions $c_{0,1} = 0.5$, $c_{0,2} = c_{0,3} = 0$, and $c_{0,4} = 1$ serves

as an example. Fig. 2(a) corresponds to the initial conditions, Fig. 2(b) and Fig. 2(c) depict the time evolution of the analytical and finite-difference solutions, and Fig. 2(d) demonstrates that both the analytical and the finite-difference solutions tend to the steady-state solution as time tends to infinity.

B. Relaxation to steady state

The standard measure of the relaxation rate is in terms of the principal non-zero eigenvalue of the negative Laplacian [38]. Here, we obtain a similar result in terms of the smallest separation constant λ_1 . To this end, the function $\delta(t)$ depicted in Fig. 3(a) is introduced to measure the agreement between the analytical solution at time t and the steady-state solution:

$$\delta(t) = \frac{1}{\tilde{x}_2 - \tilde{x}_0} \|c(x, t) - c_s(x)\|_2^2. \quad (44)$$

Due to the analytical solution exhibiting exponential decay, the following asymptotic equivalence holds for $\delta(t)$:

$$\delta(t) \sim C \exp\left(-\frac{t}{\tau_s}\right) \quad \text{as } t \rightarrow \infty, \quad (45)$$

where C is a non-zero constant and τ_s is the time constant. The time constant τ_s , which is the measure of the relaxation rate, was calculated for different values of D_2 using data depicted in Fig. 3(a). In Fig. 3(b) we compare it with the reciprocal of the separation constant λ_1 , which demonstrates that the time constant is indeed the smallest separation constant reciprocal of the analytical solution expansion, i.e., $\tau_s = 1/\lambda_1$. Hence, the relaxation rate can be expressed in terms of the smallest separation constant λ_1 and is inversely proportional to D_2 .

C. Finite difference numerical method

The numerical solution of the diffusion equation (1) can be obtained using the finite difference method (FDM). In the present case, we will compare our quantum algorithm also with a classical numerical integration scheme. With respect to the quality of conservation, two types of FDM schemes can be distinguished, conservative and non-conservative. Although the non-conservative FDM may converge faster than the conservative FDM for smooth solutions, it fails to correctly capture discontinuities [39]. Since discontinuities arise in Eq. (1) due to discontinuous diffusivity profile, we employ conservative FDM.

First, the problem is discretized uniformly in space and time, so that $x_j = x_0 + j\Delta x$ and $t_l = t_0 + l\Delta t$, with $x_0 = 0$ and $t_0 = 0$. The indices j and l satisfy $j = 0, \dots, N+1$ and $l = 0, \dots, M$. The spatial interval $x \in [\tilde{x}_0, \tilde{x}_m]$ is divided into N interior and 2 boundary nodes; therefore, $\Delta x = (\tilde{x}_m - \tilde{x}_0) / (N+1)$. To obtain the conservative

scheme, the time derivative is discretized by a forward finite difference, while the outer and inner spatial derivatives are discretized by a central finite difference. The fluxes are evaluated at the staggered points $x_{j-\frac{1}{2}}$ and $x_{j+\frac{1}{2}}$, and subsequently approximated using concentrations at the grid points:

$$\frac{c_j^{l+1} - c_j^l}{\Delta t} = \frac{1}{\Delta x^2} \left[D_{j+\frac{1}{2}} (c_{j+1}^l - c_j^l) - D_{j-\frac{1}{2}} (c_j^l - c_{j-1}^l) \right]. \quad (46)$$

Defining

$$r_j = \frac{D_j \Delta t}{\Delta x^2} \quad \text{and} \quad s_j = 1 - \frac{D_{j+\frac{1}{2}} \Delta t}{\Delta x^2} - \frac{D_{j-\frac{1}{2}} \Delta t}{\Delta x^2} \quad (47)$$

allows for a more explicit expression:

$$c_j^{l+1} = r_{j+\frac{1}{2}} c_{j+1}^l + s_j c_j^l + r_{j-\frac{1}{2}} c_{j-1}^l. \quad (48)$$

The scheme can be expressed as a system of linear equations:

$$c^{l+1} = A c^l, \quad (49)$$

where matrix $A \in \mathbb{R}^{(N+2) \times (N+2)}$ has the following structure

$$A = \begin{bmatrix} 1 & 0 & 0 & 0 & \dots & 0 & 0 & 0 \\ r_{\frac{1}{2}} & s_1 & r_{\frac{3}{2}} & 0 & \dots & 0 & 0 & 0 \\ 0 & r_{\frac{3}{2}} & s_2 & r_{\frac{5}{2}} & \dots & 0 & 0 & 0 \\ \vdots & \vdots & \ddots & \ddots & \ddots & \vdots & \vdots & \vdots \\ 0 & 0 & 0 & 0 & \dots & r_{N-\frac{1}{2}} & s_N & r_{N+\frac{1}{2}} \\ 0 & 0 & 0 & 0 & \dots & 0 & 0 & 1 \end{bmatrix}. \quad (50)$$

The first and the last rows of A serve to incorporate the inhomogeneous Dirichlet boundary conditions located at c_0^l and c_{N+1}^l . To ensure that this scheme is stable, the generalization of the Courant–Friedrichs–Lewy (CFL) condition, namely, the principle of frozen coefficients is used, i.e.:

$$\Delta t < \frac{\Delta x^2}{2 \max_x D(x)}. \quad (51)$$

It was proven in ref. [40] that the CFL condition is sufficient for the conservative scheme applied to the diffusion equation with discontinuous coefficients.

III. VARIATIONAL QUANTUM ALGORITHM

A. Weak formulation framework including boundary conditions

We apply the weak formulation proposed by Bengoechea et al. [26]. For the approach to be applicable to the problem (1), it must be slightly reformulated by recognizing that the charge profile $c(x, t)$ can be decomposed

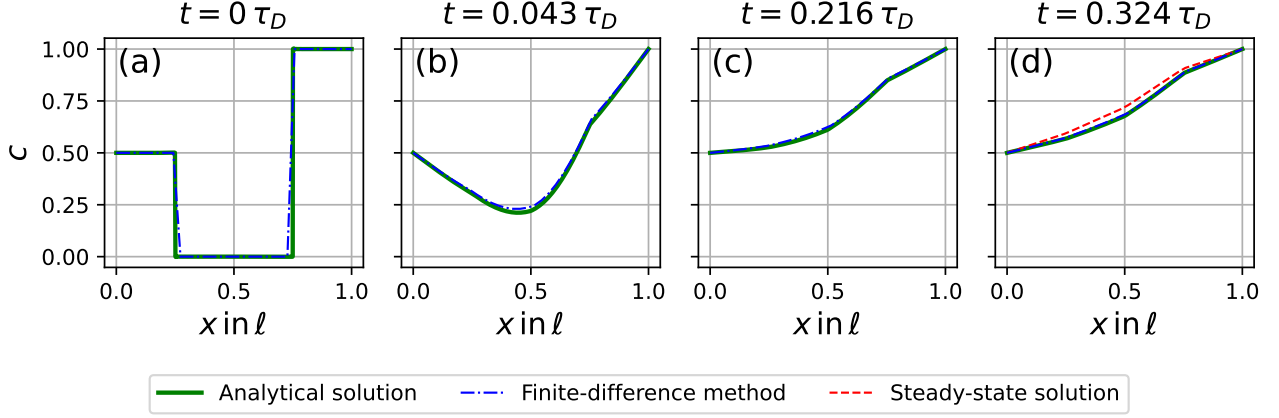


FIG. 2: Analytical solution compared at different time instants together with the finite-difference solution. Panel (a) shows the initial conditions, panels (b) and (c) depict time evolution at different time instants, and panel (d) demonstrates how the analytical and numerical finite-difference solutions tend to the steady-state solution.

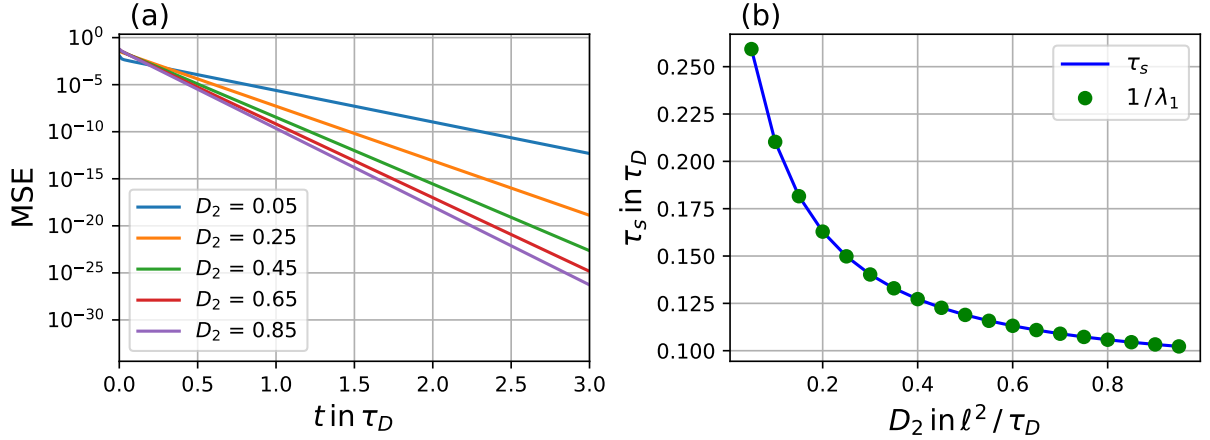


FIG. 3: Relaxation rate analysis of the problem. (a) The function $\delta(t)$ for various values of D_2 . (b) The time constant τ_s and smallest positive eigenvalue reciprocals for various values of D_2 .

into two components, namely, the steady-state solution and the transient solution:

$$c(x, t) = c_s(x) + \tilde{c}(x, t), \quad (52)$$

where $\tilde{c}(x, t)$ is the transient solution. Then, eq. (1) is reformulated in terms of the transient solution $\tilde{c}(x, t)$:

$$\frac{\partial \tilde{c}}{\partial t} = \frac{\partial}{\partial x} \left(D(x) \frac{\partial \tilde{c}}{\partial x} \right) \quad \text{in } \Omega_T = (\tilde{x}_0, \tilde{x}_m) \times (0, T] \quad (53)$$

with the following initial,

$$\tilde{c}(x, 0) = c_0(x) - c_s(x), \quad (54)$$

and homogeneous Dirichlet boundary conditions,

$$\tilde{c}(\tilde{x}_0, t) = 0 \quad \text{and} \quad \tilde{c}(\tilde{x}_m, t) = 0. \quad (55)$$

Equation (53), expressed in terms of the transient solution $\tilde{c}(x, t)$, is now ready to be reformulated as a finite-dimensional optimization problem. The time derivative

is approximated using the backward finite difference formula:

$$\frac{\partial \tilde{c}}{\partial t} = \frac{\tilde{c}^l - \tilde{c}^{l-1}}{\Delta t} + \mathcal{O}(\Delta t) \quad (56)$$

where $\tilde{c}^l = \tilde{c}^l(x)$ is the spatial charge profile at l -th time instant, and Δt is the integration time step. Therefore, the PDE is approximated by a second-order linear system of ODEs:

$$\tilde{c}^l - \Delta t \frac{d}{dx} \left(D(x) \frac{d\tilde{c}^l}{dx} \right) = \tilde{c}^{l-1} \quad (57)$$

The weak formulation of the obtained system of ODEs is given by

$$\underbrace{\int_{\Omega} v^l \left[\frac{\tilde{c}^l}{\Delta t} - \frac{d}{dx} \left(D(x) \frac{d\tilde{c}^l}{dx} \right) \right] dx}_{a(v^l, \tilde{c}^l)} = \underbrace{\int_{\Omega} v^l \frac{\tilde{c}^{l-1}}{\Delta t} dx}_{f(v^l)}, \quad (58)$$

for all test functions $v^l \in V$. Here, $a(v^l, \tilde{c}^l)$ is a symmetric and positive definite bilinear form and $f(v^l)$ is a linear form. The weak formulation above is equivalent to the following optimization problem,

$$\min_{\tilde{c}^l \in V} \left[\frac{1}{2} a(\tilde{c}^l, \tilde{c}^l) - f(\tilde{c}^l) \right]. \quad (59)$$

According to the Ritz-Galerkin method, the space V is replaced with a finite-dimensional space \mathbb{R}^N , leading to a finite-dimensional optimization problem. Approximating integrals in $a(\tilde{c}^l, \tilde{c}^l)$ and $f(\tilde{c}^l)$ using the midpoint rule results in:

$$\min_{\tilde{c}^l \in \mathbb{R}^N} \left\{ \frac{\Delta x}{2\Delta t} \sum_{j=1}^N [\tilde{c}_j^l]^2 - \frac{\Delta x}{2} \sum_{j=1}^N \tilde{c}_j^l \left[\frac{d}{dx} \left(D(x) \frac{d\tilde{c}^l}{dx} \right) \right] \Big|_{x=x_j} - \frac{\Delta x}{\Delta t} \underbrace{\sum_{j=1}^N \tilde{c}_j^{l-1} \tilde{c}_j^l}_{S_{\text{LIN}}(\tilde{c}^l)} \right\}. \quad (60)$$

The diffusion operator in (60) is discretized by successive application of the central finite difference formula at staggered (outer derivative) and collocated (inner derivatives) points. This results in

$$\begin{aligned} & \left[\frac{d}{dx} \left(D(x) \frac{d\tilde{c}^l}{dx} \right) \right] \Big|_{x=x_j} \\ &= \frac{D_{j+\frac{1}{2}} \frac{d\tilde{c}^l}{dx} \Big|_{x=x_{j+\frac{1}{2}}} - D_{j-\frac{1}{2}} \frac{d\tilde{c}^l}{dx} \Big|_{x=x_{j-\frac{1}{2}}}}{\Delta x} \\ &= \frac{D_{j+\frac{1}{2}} (\tilde{c}_{j+1}^l - \tilde{c}_j^l) - D_{j-\frac{1}{2}} (\tilde{c}_j^l - \tilde{c}_{j-1}^l)}{\Delta x^2} \\ &= \frac{D_{j-\frac{1}{2}} \tilde{c}_{j-1}^l - (D_{j-\frac{1}{2}} + D_{j+\frac{1}{2}}) \tilde{c}_j^l + D_{j+\frac{1}{2}} \tilde{c}_{j+1}^l}{\Delta x^2}. \end{aligned}$$

Then the second sum in (60) becomes:

$$\begin{aligned} & \sum_{j=1}^N \tilde{c}_j^l \left[\frac{d}{dx} \left(D(x) \frac{d\tilde{c}^l}{dx} \right) \right] \Big|_{x=x_j} = \frac{1}{\Delta x^2} \sum_{j=1}^N \tilde{c}_j^l D_{j+\frac{1}{2}} \tilde{c}_{j+1}^l \\ & - \frac{1}{\Delta x^2} \underbrace{\sum_{j=1}^N \tilde{c}_j^l (D_{j-\frac{1}{2}} + D_{j+\frac{1}{2}}) \tilde{c}_j^l}_{S^{\pm}(\tilde{c}^l)} \\ & + \frac{1}{\Delta x^2} \sum_{j=1}^N \tilde{c}_j^l D_{j-\frac{1}{2}} \tilde{c}_{j-1}^l. \end{aligned}$$

Since the transient solution $\tilde{c}(x, t)$ is subject to homogeneous Dirichlet conditions $\tilde{c}_0 = \tilde{c}_{N+1} = 0$, the first and

the last sums in the equation above can be combined as:

$$\begin{aligned} S_{\text{DIR}}(\tilde{c}^l) &= \sum_{j=1}^N \tilde{c}_j^l D_{j+\frac{1}{2}} \tilde{c}_{j+1}^l + \sum_{j=1}^N \tilde{c}_j^l D_{j-\frac{1}{2}} \tilde{c}_{j-1}^l \\ &= \left(\underbrace{\tilde{c}_N^l D_{N+\frac{1}{2}} \tilde{c}_{N+1}^l}_{=0} + \sum_{j=1}^{N-1} \tilde{c}_j^l D_{j+\frac{1}{2}} \tilde{c}_{j+1}^l \right) \\ &+ \left(\underbrace{\tilde{c}_0^l D_{\frac{1}{2}} \tilde{c}_1^l}_{=0} + \sum_{j=1}^{N-1} \tilde{c}_j^l D_{j+\frac{1}{2}} \tilde{c}_{j+1}^l \right) \\ &= 2 \sum_{j=1}^{N-1} \tilde{c}_j^l D_{j+\frac{1}{2}} \tilde{c}_{j+1}^l. \end{aligned}$$

The desired Dirichlet sum S_{DIR} is challenging to evaluate directly on a quantum computer due to its incorporation of boundary conditions that break translational symmetry. Bengoechea et al. [26] propose decomposing this sum into a periodic one,

$$S_{\text{PER}}(\tilde{c}^l) = \tilde{c}_1 D_{N+\frac{1}{2}} \tilde{c}_N + \sum_{j=1}^{N-1} \tilde{c}_j^l D_{j+\frac{1}{2}} \tilde{c}_{j+1}^l,$$

and an additional corrective term, which can be evaluated using the circuit proposed by Over et al. [27]. Therefore, the sum $S_{\text{DIR}}(\tilde{c}^l)$ is expressed in terms of the periodic sum $S_{\text{PER}}(\tilde{c}^l)$ and the corrective term $S_{\text{BND}}(\tilde{c}^l)$:

$$S_{\text{DIR}}(\tilde{c}^l) = 2S_{\text{PER}}(\tilde{c}^l) - \underbrace{2\tilde{c}_1 D_{N+\frac{1}{2}} \tilde{c}_N}_{S_{\text{BND}}(\tilde{c}^l)}.$$

Then, the sum involving the diffusion operator evaluated at nodes becomes

$$\begin{aligned} & \sum_{j=1}^N \tilde{c}_j^l \left[\frac{d}{dx} \left(D(x) \frac{d\tilde{c}^l}{dx} \right) \right] \Big|_{x=x_j} \\ &= \frac{1}{\Delta x^2} S_{\text{DIR}}(\tilde{c}^l) - \frac{1}{\Delta x^2} S^{\pm}(\tilde{c}^l) \\ &= \frac{2}{\Delta x^2} \left[S_{\text{PER}}(\tilde{c}^l) - \frac{1}{2} S_{\text{BND}}(\tilde{c}^l) \right] - \frac{1}{\Delta x^2} S^{\pm}(\tilde{c}^l). \end{aligned}$$

Substituting this result into eq. (60) gives the optimization problem with a cost function that consists of terms that can be evaluated directly using quantum circuits:

$$\begin{aligned} \min_{\tilde{c}^l \in \mathbb{R}^N} & \left\{ \frac{\Delta x}{2\Delta t} \sum_{j=1}^N [\tilde{c}_j^l]^2 - \frac{1}{\Delta x} S_{\text{PER}}(\tilde{c}^l) + \frac{1}{2\Delta x} S_{\text{BND}}(\tilde{c}^l) \right. \\ & \left. + \frac{1}{2\Delta x} S^{\pm}(\tilde{c}^l) - \frac{\Delta x}{\Delta t} S_{\text{LIN}}(\tilde{c}^l) \right\}. \end{aligned} \quad (61)$$

Since the cost function is supposed to be expressed as a function of the normalized charge profile $\hat{c}^l \in \mathbb{R}^N$ the following substitution is made:

$$\tilde{c}_j^l = \lambda_0 \hat{c}_j^l, \quad j = 1, \dots, N, \quad (62)$$

where λ_0^l is the normalization constant and $\|\hat{c}^l\|_2 = 1$. Finally, the transformed version of the optimization problem (60) suitable for an implementation as a VQA algorithm is given by

$$\min_{\lambda_0^l \in \mathbb{R}, \hat{c}^l \in \mathbb{R}^N} \left\{ \frac{\Delta x}{2\Delta t} [\lambda_0^l]^2 - \frac{1}{\Delta x} [\lambda_0^l]^2 S_{\text{PER}}(\hat{c}^l) + \frac{1}{2\Delta x} [\lambda_0^l]^2 S_{\text{BND}}(\hat{c}^l) + \frac{1}{2\Delta x} [\lambda_0^l]^2 S^\pm(\hat{c}^l) - \frac{\Delta x}{\Delta t} \lambda_0^{l-1} \lambda_0^l S_{\text{LIN}}(\hat{c}^l) \right\}. \quad (63)$$

The normalized charge profile \hat{c}^l is generated by a parameterized quantum circuit, that is, it depends on the parameter vector λ

$$\hat{c}^l = \hat{c}(\lambda^l) = U(\lambda^l)|0\rangle^{\otimes n}. \quad (64)$$

Each term S_{PER} , S^\pm , S_{LIN} and S_{BND} is computed using a corresponding Hadamard test circuit, see also the appendix of ref. [25]. The circuit diagrams for computing S_{PER} , S^\pm and S_{LIN} are displayed in Fig. 4. The quantum circuit for S_{DIR} is introduced in [27]. The first register containing a single qubit is an ancillary qubit of the Hadamard test. The solution register allows loading the amplitude encoding of the charge concentrations and performing operations on them. The purpose of the coefficient register is to introduce the coefficients of the quadratic forms S_{PER} and S^\pm . There, the P unitary is nothing else but state preparation circuits that prepare states proportional to $(D_{\frac{3}{2}}, D_{\frac{5}{2}}, \dots, D_{N+\frac{1}{2}})$ for S_{PER} and $(D_{\frac{1}{2}} + D_{\frac{3}{2}}, D_{\frac{3}{2}} + D_{\frac{5}{2}}, \dots, D_{N-\frac{1}{2}} + D_{N+\frac{1}{2}})$ for S^\pm respectively. When computing S^\pm , the shift block \hat{S}_- is omitted. The next section will introduce the quantum state preparation algorithm for such states.

B. Quantum state preparation algorithm

In this section, we present the quantum state preparation algorithm designed to encode the coefficients of quadratic forms in the VQA cost function. The necessity of this specific state preparation algorithm arises from the structure of these coefficient vectors, which predominantly consist of a small number of constant subvectors, a property directly resulting from the piecewise-constant nature of the diffusion coefficient. By exploiting this structure, our algorithm generates quantum circuits with significantly fewer gates compared to general-purpose state preparation methods.

1. Successive bisection

The underlying principle of the algorithm employs a recursive dichotomy process: starting with an initial con-

stant vector, the procedure iteratively bisects it into constant subsegments using a finite number of iterations until the constructed vector precisely matches the desired target state. In each iteration, the process ensures that the approximation resulting from the bisection can be progressively refined in subsequent iterations. This is achieved by guaranteeing that when a segment is bisected, its magnitude is redistributed among its constant subsegments, such that they approximate the desired vector in an average sense. At the end of the process, the approximated vector is equal to the desired vector element-wise.

Figure 5(a)-(d) provides an example of an 8-dimensional vector illustrating this principle. The desired vector is shown in Figure 5(d), it consists of a 3-element constant segment followed by a 5-element constant segment. To arrive at the desired vector, one starts with a constant vector as in Figure 5(a). Its magnitude is set equal to the combined magnitude of the target vector, i.e., $S_1 = 3A + B + C$. To approximate the desired vector, the initial constant vector is bisected into two segments S_{21} and S_{22} , which are separated by moving S_{21} upward and S_{22} downward. This produces the first approximation of the desired vector shown in Figure 5(b). As can be seen, the magnitude of the left segment is $S_{21} = 3A + B$ and the magnitude of the right segment is $S_{22} = C$. The first approximation is then compared with the desired vector to determine which segments of it have to be further bisected. For example, bisecting S_{22} is not necessary, because its counterpart in the desired vector is already constant, and there is no need to redistribute the magnitude of S_{22} . The left segment S_{21} in the first approximation, however, has to be bisected, because it should eventually exhibit a discontinuity as in the desired vector. Thus, bisecting and separating S_{21} produces the second approximation shown in Figure 5(c), where the magnitude S_{21} is redistributed between the subsegments with magnitudes $S_{31} = 2A$ and $S_{32} = A + B$, respectively. Now, the subsegments S_{31} and S_{32} are compared with their counterparts in the desired vector. The subsegment S_{31} does not have to be bisected, as its counterpart in the desired vector is already constant, thus it is left unchanged. The subsegment S_{32} , on the other hand, has to be bisected, as its counterpart in the desired vector has a discontinuity. Since S_{32} is a two-element subsegment, it is bisected into two one-element subsegments with magnitudes A and B , or, equivalently, two individual amplitudes with values \sqrt{A} and \sqrt{B} . Therefore, bisecting S_{32} produces the third and final approximation, which reproduces the desired vector exactly.

The example described above can be generalized into the following procedure: for each marked constant segment in the current approximation, (1) check if its counterpart in the desired vector contains a discontinuity; if so, (2) bisect the segment into two smaller constant subsegments ensuring correct magnitudes, and (3) mark the subsegments for the next iteration.

We now formalize this procedure using the quantum

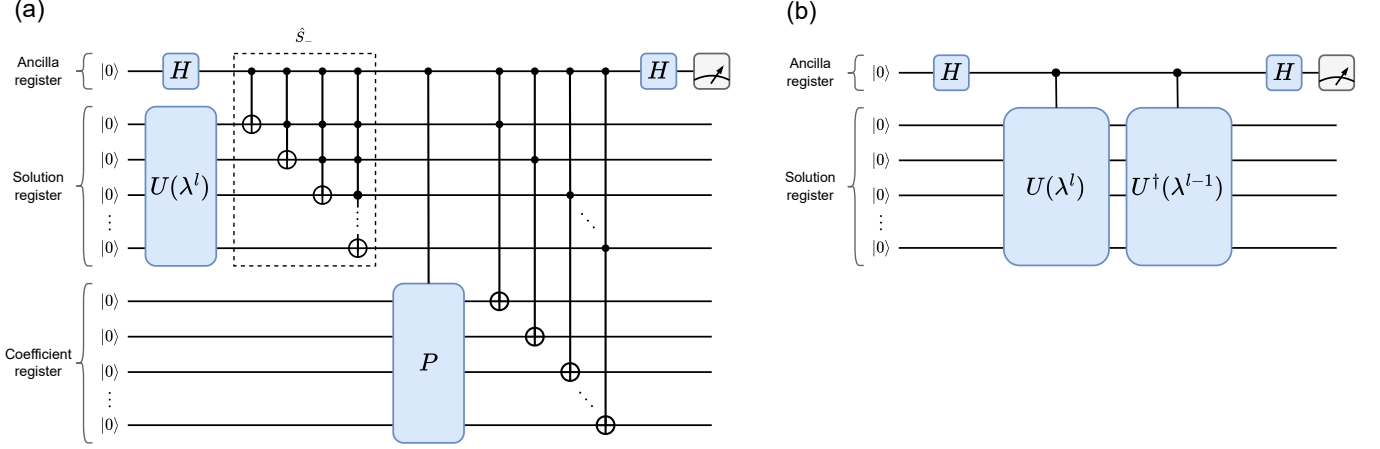


FIG. 4: Quantum circuits for computing individual terms of the cost function. Circuit (a) evaluates the terms S_{PER} and S^{\pm} , where the unitary P incorporates the respective coefficients. Circuit (b) evaluates the term S_{LIN} .

state notation. Suppose a desired real-valued quantum state $|\psi\rangle \in \mathbb{C}^N$ containing normalized coefficients of a quadratic form is given. If it contains a discontinuity, which is the case for the given state, it is split into two partial states $|\tilde{\psi}_0\rangle$ and $|\tilde{\psi}_1\rangle$ with respect to the most significant qubit, i.e.,

$$|\psi\rangle = |0\rangle \otimes |\tilde{\psi}_0\rangle + |1\rangle \otimes |\tilde{\psi}_1\rangle. \quad (65)$$

Then, the state $|\phi\rangle$, which is the first approximation of $|\psi\rangle$, is introduced and initialized such that

$$|\phi\rangle \leftarrow \sqrt{\langle \tilde{\psi}_0 | \tilde{\psi}_0 \rangle} |0\rangle \otimes |\tilde{\phi}_0\rangle + \sqrt{\langle \tilde{\psi}_1 | \tilde{\psi}_1 \rangle} |1\rangle \otimes |\tilde{\phi}_1\rangle, \quad (66)$$

with

$$|\tilde{\phi}_0\rangle \leftarrow |+\rangle^{\otimes(n-1)} \quad \text{and} \quad |\tilde{\phi}_1\rangle \leftarrow |+\rangle^{\otimes(n-1)}. \quad (67)$$

Therefore, in the first iteration, $|\psi\rangle$ is approximated by $|\phi\rangle$, which consists of two uniform superpositions, such that their norms are equal to those of $|\tilde{\psi}_0\rangle$ and $|\tilde{\psi}_1\rangle$. Figure 5(e) with blocks B_1 , B_2 and B_{n-1} being omitted, shows the circuit for preparing the state $|\phi\rangle$. The amplitudes of the partial states $|\tilde{\phi}_0\rangle$ and $|\tilde{\phi}_1\rangle$ in $|\phi\rangle$ are assigned using a rotation about the y -axis (R_Y) acting on the most significant qubit q_{n-1} , while partial states $|\tilde{\phi}_0\rangle$ and $|\tilde{\phi}_1\rangle$ themselves are generated using the Hadamard gates acting on qubits q_0, q_1, \dots, q_{n-2} . Application of the R_Y gate can be thought of as redistributing the unit norm of the initial uniform superposition between two constant segments as in Figs 5(a)-(b). Pairs of states $(|\tilde{\psi}_0\rangle, |\tilde{\phi}_0\rangle)$ and $(|\tilde{\psi}_1\rangle, |\tilde{\phi}_1\rangle)$ are then marked as the ones requiring further processing. In the second iteration, the marked states $|\tilde{\psi}_0\rangle$ and $|\tilde{\psi}_1\rangle$ are checked for discontinuities. If among the marked states there are ones containing discontinuities, the algorithm proceeds further by splitting these states, denoted as $|\tilde{\psi}_j\rangle$ (where $j \in \{0, 1\}$), analogously to eq. (65),

$$|\tilde{\psi}_j\rangle = |0\rangle \otimes |\tilde{\psi}_{j0}\rangle + |1\rangle \otimes |\tilde{\psi}_{j1}\rangle. \quad (68)$$

and the state $|\phi\rangle$ is updated by bisecting the partial state $|\tilde{\phi}_j\rangle$ as,

$$|\tilde{\phi}_j\rangle \leftarrow \sqrt{\frac{\langle \tilde{\psi}_{j0} | \tilde{\psi}_{j0} \rangle}{\langle \tilde{\psi}_j | \tilde{\psi}_j \rangle}} |0\rangle \otimes |\tilde{\phi}_{j0}\rangle + \sqrt{\frac{\langle \tilde{\psi}_{j1} | \tilde{\psi}_{j1} \rangle}{\langle \tilde{\psi}_j | \tilde{\psi}_j \rangle}} |1\rangle \otimes |\tilde{\phi}_{j1}\rangle,$$

with

$$|\tilde{\phi}_{j0}\rangle \leftarrow |+\rangle^{\otimes(n-2)} \quad \text{and} \quad |\tilde{\phi}_{j1}\rangle \leftarrow |+\rangle^{\otimes(n-2)}, \quad (69)$$

whereas pairs of states $(|\tilde{\psi}_{j0}\rangle, |\tilde{\phi}_{j0}\rangle)$ and $(|\tilde{\psi}_{j1}\rangle, |\tilde{\phi}_{j1}\rangle)$ are marked for the next iteration. For example, if the state in Figure 5(d) is to be generated, the partial state $|\tilde{\phi}_0\rangle$ is bisected in the second iteration, as it corresponds to the left subsegment S_{21} . The updated state $|\phi\rangle$ is generated by introducing the block B_1 in the circuit in Figure 5(e). Depending on which partial states $|\tilde{\phi}_j\rangle$ have to be bisected, corresponding controlled R_Y gates are introduced, such that they act on qubit q_{n-2} and controlled by qubit q_{n-1} , while conditioned by the computational state $|j\rangle$. Similarly, in the third iteration, partial states $|\tilde{\psi}_{j0}\rangle$ and $|\tilde{\psi}_{j1}\rangle$ are checked for discontinuities, and for states $|\tilde{\psi}_{jk}\rangle$ (with $(j, k) \in \{0, 1\}^2$) containing discontinuities, corresponding states $|\tilde{\phi}_{jk}\rangle$ are bisected. However, this time the block B_2 is introduced, where multi-controlled R_Y (MCRY) gates are conditioned by the state $|jk\rangle$. Therefore, starting from the third iteration, the process is similar except that MCRY gates are used to carry out the bisection process. The complete algorithm is presented in Algorithm 1.

2. Gate complexity estimate

A circuit generated by Algorithm 1 requires three types of components, namely, single-qubit R_Y , Hadamard H , and MCRY gates. From the algorithmic description of the procedure, it is clear that there is one single-qubit

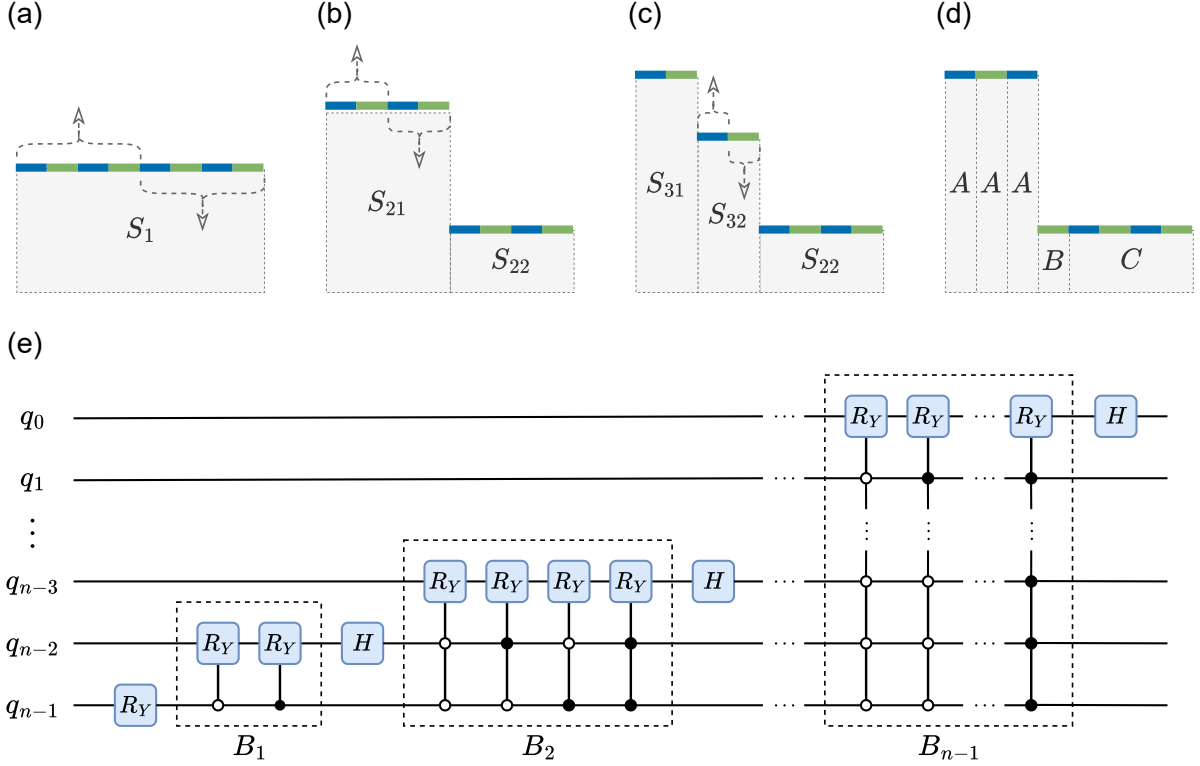


FIG. 5: Sketch of the principle of the state preparation algorithm shown in panels (a)-(d) and a general quantum circuit produced by the state preparation algorithm shown in panel (e). The arrows in panels (a)-(d) indicate the direction in which each corresponding segment is shifted — either upward or downward. Gray rectangles with dashed borders depict the areas under the various segments. In panels (e), blocks B_1 and B_2 produce the second and the third approximations of the desired state, respectively. Block B_{n-1} produces the final approximation.

R_Y rotation gate and $n - 1$ Hadamard gates, and their combined gate complexity is, therefore, $O(n)$. The combined gate complexity of all MCRY gates is, however, less straightforward. On the one hand, there are $n - 1$ iterations of the outer loop in which MCRY gates might be applied. On the other hand, interpreting $|\psi\rangle$ as a piecewise-constant vector consisting of p parts, the number of MCRY gates applied in each iteration is at most $p - 1$. This is due to the fact that starting from the second iteration of the outer loop of Algorithm 1, at most $p - 1$ non-uniform parts will be present in $\tilde{\Psi}$, each requiring one MCRY gate. Therefore, there are at most $(p - 1)(n - 1)$ MCRY gates in total. A k -qubit MCRY gate can be implemented using $O(k)$ CNOT and single-qubit gates [41]. The gate complexity of any k -qubit MCRY gate in Algorithm 1, for simplicity, can be bounded from above by the complexity of the n -qubit MCRY gate, since $n \geq k$. Since there are now $(p - 1)(n - 1)$ MCRY gates, each requiring $O(n)$ single-qubit and CNOT gates, the combined gate complexity of all MCRY gates is $O(pn^2)$. Because the combined gate complexity of the other gates is only $O(n)$, the gate complexity of the entire state preparation circuit is $O(pn^2)$. This complexity is significantly lower than that of general state preparation methods, which

typically have exponential complexity $O(2^n)$.

It is worth pointing out, that the actual gate complexity also depends on how amplitudes in $|\psi\rangle$ are arranged and can be reduced drastically in special cases, e.g., when $|\psi\rangle$ is comprised of p equally-sized parts, in which case the gate complexity can be reduced to $O(pn)$. The gate complexity $O(pn^2)$ obtained above corresponds to the worst case.

IV. RESULTS

In the following, we present the results of the VQA simulations. They are performed with the quantum simulation software Qiskit version 1 [42] in ideal statevector simulations applying 4 to 6 qubit ansatz circuits. Before we discuss the performance of the quantum algorithm, we investigate the expressibility of the ansatz circuit and the classical optimization algorithms which have been compared in our study.

Algorithm 1: State preparation algorithm

input : A vector of real amplitudes ψ of size $n \geq 1$
 such that $\|\psi\|_2 = 1$
output: State preparation circuit
 $d \leftarrow n$;
while $d \neq 0$ **do**
 $\tilde{\Psi} \leftarrow \emptyset$;
 /* Process each state ψ in Ψ */
 foreach $\psi \in \Psi$ **do**
 if *IsUniform*(ψ) *is False* **then**
 $j \leftarrow \text{Subscript}(\text{First}(\psi))$;
 /* Split ψ into two parts */
 $\tilde{\Psi} \leftarrow \tilde{\Psi} \cup \{(\psi_j, \dots, \psi_{j+2^{d-1}-1})\}$;
 $\tilde{\Psi} \leftarrow \tilde{\Psi} \cup \{(\psi_{j+2^{d-1}}, \dots, \psi_{j+2^d-1})\}$;
 /* Compute rotation angle */
 $u \leftarrow \sqrt{\sum_{k=j}^{j+2^{d-1}-1} \psi_k^2}$;
 $v \leftarrow \sqrt{\sum_{k=j}^{j+2^d-1} \psi_k^2}$;
 $\theta \leftarrow 2 \arccos(u/v)$;
 if $d = n$ **then**
 Apply MCRY gate with angle θ to
 qubit $(d-1)$;
 else
 Apply MCRY gate with angle $(\theta - \pi/2)$
 to qubit $(d-1)$ controlled by qubits
 $(n-1)$ through d in state $|\text{bin}(j)\rangle$;
 if $d > 1$ **then**
 Apply Hadamard gate to qubit $(d-2)$;
 $\Psi \leftarrow \tilde{\Psi}$;
 $d \leftarrow d-1$;
end while

A. Expressibility of parametric quantum circuit

To encode the transient charge profile $\tilde{c}(x, t)$ in the VQA, the real-valued parametric quantum circuit (RPQC) with reverse linear entanglement was selected from the Qiskit circuit library. As depicted in Fig. 6(a), this circuit consists of an initial layer of R_Y gates followed by d layers of alternating CNOT and R_Y gates, resulting in a quantum state with real-valued probability amplitudes. Given n qubits, the number of parameters in the RPQC is $n(d+1)$.

We analyze the expressibility of the RPQC to find an optimal selection of its depth, d . The expressibility of a circuit is defined as the ability to explore the Hilbert space through an entangled unitary circuit. In general, it can be quantified using the Kullback-Leibler divergence D_{KL} of two probability density functions (PDF) [37], the distribution of fidelities $0 \leq F \leq 1$ of Haar random states $P_{\text{Haar}}(F)$ and the distribution of F resulting from the PQC, denoted as $P_{\text{RPQC}}(F; \lambda)$. For the ensemble of Haar random states, the analytical form of the PDF of fidelities [43] is $P_{\text{Haar}}(F) = (N-1)(1-F)^{N-2}$ with $N = 2^n$.

Therefore, the measure of expressibility is:

$$D_{\text{KL}} = \int_0^1 P_{\text{RPQC}}(F; \lambda) \log \left(\frac{P_{\text{RPQC}}(F; \lambda)}{P_{\text{Haar}}(F)} \right) dF \quad (70)$$

Since Haar random states uniformly sample the Hilbert space of pure states, the smaller the D_{KL} , the better the states generated by the RPQC approximate this uniform distribution over the space, and therefore, the higher the expressibility of the RPQC. The $P_{\text{RPQC}}(F; \lambda)$ PDF is calculated as follows (see also ref. [31]): (1) Q pairs of parameter vectors λ_1 and λ_2 are sampled uniformly and independently; (2) the RPQC is used to generate the corresponding states $|\psi(\lambda_1)\rangle = U(\lambda_1)|0\rangle$ and $|\psi(\lambda_2)\rangle = U(\lambda_2)|0\rangle$; (3) their fidelities $F = |\langle\psi(\lambda_1)|\psi(\lambda_2)\rangle|^2$ are calculated; (4) $P_{\text{RPQC}}(F; \lambda)$ is approximated using the probability density histogram of the previously obtained fidelities F . Figure 6(b) displays the results for D_{KL} for the 6-qubit RPQC as a function of the circuit depth d . The number of bins used to obtain the probability density histogram is 320. The number of quantum state pairs is given in the legend. It can be seen that D_{KL} decays with increasing d and saturates for $d \geq 4$, $d \geq 5$ and $d \geq 6$ for 4-, 5- and 6-qubit ansätze respectively. The number of pairs, Q , has been varied from 10^4 to 5×10^5 , which did not change the result. We use D_{KL} as a general measure, for simplicity. The ansatz circuit is thus a problem-agnostic choice and does not incorporate application-specific properties.

B. Adaption of surrogate-based optimization

The classical optimization algorithms, such as the Nelder–Mead (NM) [44], the Broyden–Fletcher–Goldfarb–Shanno (BFGS), and a surrogate-based optimization with kernel approximations (SBO) [35], were used for detecting the minimum of the VQA cost function.

The idea behind the latter SBO algorithm is to approximate the cost function based on its τ random samples within a hypercube of length ℓ^0 centered around an initial guess $\theta^0 = (\theta_0^0, \theta_1^0, \dots, \theta_M^0)$ of the variational parameters. The obtained approximation is then optimized classically subject to the box-constraints corresponding to the hypercube. Once the local minimum is found, it becomes the center of the next hypercube of smaller length ℓ^1 and the process repeats. The algorithm requires a user to provide parameter values including among others the size of the initial hypercube ℓ^0 , the number of points τ to sample within each hypercube, and the number of iterations n_{iter} . As suggested by the original paper, τ is kept fixed. For setting n_{iter} , we use a simple heuristic formula,

$$n_{\text{iter}} = \left\lceil \frac{n_{\text{fev}}}{\tau} \right\rceil, \quad (71)$$

where n_{fev} is the overall function evaluation budget. For setting the initial hypercube length ℓ^0 , we use two approaches. In the first, ℓ^0 is set to $\|\theta_1 - \theta_0\|_\infty$ for all time

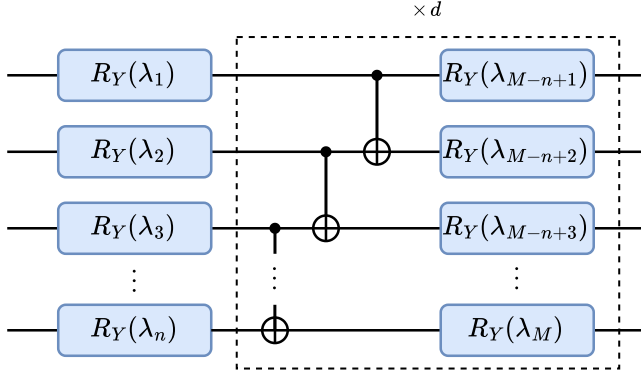


FIG. 6: Real-valued parametric quantum circuit (RPQC) and its expressibility in terms of the Kullback-Leibler divergence. Left panel shows the RPQC from the Qiskit circuit library with reverse linear entanglement and d layers. Right panel shows expressibility of the RPQC as a function of the depth d for 4-, 5-, and 6-qubit ansätze. The legend displays the number of pairs Q that have been generated.

steps, meaning that the hypercube contains the solution to the next time step, since $\|\theta_1 - \theta_0\|_\infty \geq \|\theta_{j+1} - \theta_j\|_\infty$ assuming that RPQC is expressible enough. We call this approach fixed patch size (FPS). The second approach, called heuristic patch size (HPS), sets the patch size according to the number of iterations n_{iter} and the number of variational parameters $M+1$ such that the maximum Euclidean distance that the algorithm can cover within n_{iter} iterations is proportional to $\|\theta_1 - \theta_0\|_2$. Namely, in each iteration of the optimization algorithm the maximum distance covered by the algorithm is a half diagonal of the hypercube, as depicted in Fig. 7, and thus

$$\max \|\Delta \theta^i\| = \frac{\sqrt{M+1}}{2} \ell^i. \quad (72)$$

Taking that into account that $\ell^i = \ell^0(1 - i/n_{\text{iter}})$, the total maximum distance covered by the algorithm is given by

$$\max \|\Delta \theta\|_2 = \frac{\sqrt{M+1}(n_{\text{iter}} + 1)}{4} \ell^0. \quad (73)$$

Therefore, requiring that $\max \|\Delta \theta\|_2 = \|\theta_1 - \theta_0\|_2$, the initial patch size can now be defined in terms of the maximum distance between two consecutive variational parameter sets:

$$\ell^0 = \frac{4(\gamma + 1)\|\theta_1 - \theta_0\|_2}{\sqrt{M+1}(n_{\text{iter}} + 1)}, \quad (74)$$

where $\gamma \geq 0$ is an empirical parameter that accounts for, e.g., zigzag behavior of the iterates.

The vector of the variational parameters θ used in the SBO algorithm contains $M+1$ angles in the range $[0, 2\pi]$, where the first angle should correspond to the normalization constant λ_0 from the VQA formulation. To map the

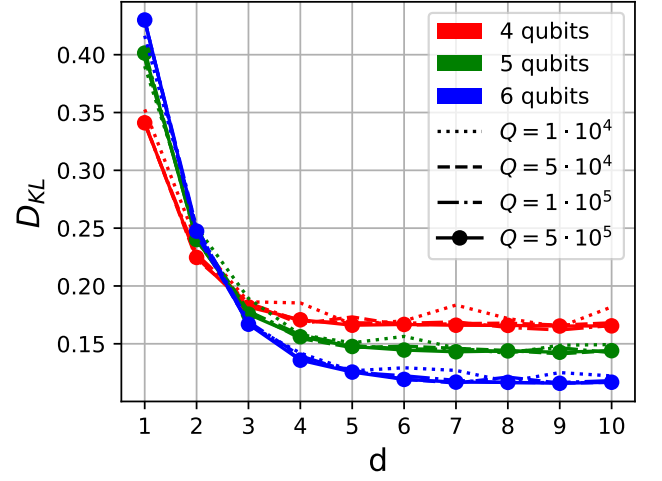


FIG. 7: Sketch of the maximum distance $\max \|\Delta \theta\|_2$ that can be covered by the surrogate-based optimization (SBO).

variational parameters (λ_0, λ) used in (62) and (64) to θ , we use the following relations:

$$\theta_0 = 2\pi \frac{\lambda_0^l}{\lambda_0^0} \quad \text{and} \quad \theta_j = \lambda_j^l, \quad j = 1, \dots, M, \quad (75)$$

where λ_0^0 and λ_0^l are normalization constants of the initial conditions and the solution at l -th time step, respectively. Since, the VQA simulates the transient solution $\tilde{c}(x, t)$, its 2-norm, or, equivalently, the normalization constant λ_0^l , is bounded from above by λ_0^0 and tends to converge to zero as $t \rightarrow \infty$, therefore, $\theta_0 \in [0, 2\pi]$, as required by

the SBO algorithm.

C. Time evolution of concentration profile

1. Quantum simulation parameters

The diffusion equation (1) was solved approximately for 100 time steps with an integration step width $\Delta t = \Delta x^2/2$ using the FDM and VQA methods with $D_1 = 1 \ell^2/\tau_D$, $D_2 = 0.01, 0.25, 0.50, 0.75 \ell^2/\tau_D$ and $N = 16, 32, 64$ with ideal state-vector simulations. The interface position \tilde{x}_1 is chosen to be $10/11 \ell$ as in Fig. 1(b), with $\tilde{x}_0 = 0 \ell$ and $\tilde{x}_2 = 1 \ell$. The ansatz circuits for the real amplitudes with $d = 4, 5$ and 6 layers were used in all 4-, 5- and 6-qubit quantum simulation experiments involving the VQA, respectively. The transient solution $\tilde{c}(x, t)$ is combined with the steady-state solution $c_s(x)$ as prescribed by (52) to produce the full ion concentration profile $c(x, t)$. This is then compared with the FDM result and the analytical solution. Recall that the analytical series solution is obtained using 30000 terms in eq. (43).

The BFGS algorithm was chosen at the beginning as the optimization routine, with a maximum number of iterations of 100 and $\|\nabla C(\theta)\|_2 < 1 \times 10^{-3}$ as the termination criterion. Figure 8 shows the mean squared error (MSE) of the FDM and VQA methods relative to the analytical solution (43).

2. Time evolution and dependence on strength of discontinuity of diffusion constant

Inspecting the graphs, one can deduce that, in terms of MSE, the FDM always performs better than the VQA. The reason is that while the VQA utilizes the same finite differences as the FDM, it uses an ansatz circuit to express the solution, which inevitably introduces error and steers the solution away from the FDM. Moreover, increasing the spatial resolution leads to a higher MSE of the VQA as opposed to the FDM when 6 qubits are employed as can be seen in Figs. 8(a)-(c). This is because even though 6 layers achieve the maximum expressibility of a 6-qubit RPQC, the number of free parameters in this case is still less than the number of grid points, which leads to the concentrations at grid points being under-determined. Figure 10 showing the concentration profile at $t = 8 \times 10^{-3} \tau_D$ for $D_2 = 0.5 \ell^2/\tau_D$ illustrates this point. Nevertheless, the capability of the VQA method to numerically solve this specific problem is demonstrated. When the number of qubits is $n = 6$, the charge profile shown in Fig. 10(b) exhibits small spatial oscillations in the region $x \in [0, 0.75] \ell$, which are absent in the case of $n = 4$ depicted in Fig. 10(a).

The MSE curves for $D_2 = 0.01 \ell^2/\tau_D$, which is depicted in Fig. 8(d), differ significantly from other cases due to a monotonic increase in MSE within time steps

$l \in [0, 40]$. This difference can be explained in parts by comparing the charge profiles for $D_2 = 0.25 \ell^2/\tau_D$ and $D_2 = 0.01 \ell^2/\tau_D$ resolved using $N = 64$ interior grid points, as shown in Fig. 9. In both cases, the initial charge distributions are piecewise constant profiles, with a sharp change at the interface \tilde{x}_1 between the two layers. For $D_2 = 0.25 \ell^2/\tau_D$, this sharp transition is maintained for approximately 5 time steps before smoothing out. This behavior corresponds to the short-term increase followed by a decrease in MSE near time step $l = 0$ observed in Fig. 8(c).

A similar trend is also evident for the MSE in the case of $D_2 = 0.50 \ell^2/\tau_D$ shown in Fig. 8(b). However, when $D_2 = 0.01 \ell^2/\tau_D$, the sharp transition in the charge profile is maintained throughout the entire simulation duration. Similar to the cases $D_2 = 0.50 \ell^2/\tau_D$ and $D_2 = 0.25 \ell^2/\tau_D$, the corresponding MSE curves in Fig. 8(d) exhibit an increase, but this increase occurs over a much longer timescale. A decrease in MSE is observed only for $n = 4$, where the larger time step allows the simulation to progress into the phase where the initially sharp transition begins to smooth out. Therefore, the lower the value of D_2 , the more pronounced and prolonged the initial increase in the MSE becomes. This observation is consistent with the fact that the relaxation rate of the system decreases as D_2 decreases, as illustrated in Fig. 3(b). A slower relaxation rate means that the sharp transition in the charge profile diffuses more slowly, prolonging the duration of elevated MSE, as is the case for $D_2 = 0.01 \ell^2/\tau_D$.

Apart from that, when $D_2 = 0.01 \ell^2/\tau_D$, the performance of the VQA closely resembles that of the FDM, with increasing spatial resolution leading to improved overall accuracy, even when employing 6 qubits. One can notice that the MSE curves of the FDM and VQA for the same number of qubits converge as D_2 decreases, as shown in Fig. 8. Moreover, the MSE curves of the FDM tend to increase as D_2 decreases. Since the VQA uses the same spatial discretization as the FDM, this suggests that for $D_2 \rightarrow 0$, the MSE of the VQA is dominated by discretization errors rather than limitations of the PQC in representing the charge profile. This explains why the VQA performs comparatively well in the low-diffusivity regime of the membrane.

3. Results for different optimization schemes

The number of iterations of the BFGS algorithm used in the VQA for various numbers of qubits and different values of D_2 is depicted in Figs. 11(a)-(b). As shown, when $D_2 = 0.01 \ell^2/\tau_D$, the BFGS algorithm requires the fewest iterations compared to other cases. For example, Fig. 11(a) illustrates that after approximately 15 time steps ($l = 15$), a single iteration of the BFGS algorithm suffices to achieve the required gradient tolerance of the cost function. Moreover, Figs. 11(a) and (b) indicate that more iterations are needed at earlier times, near the

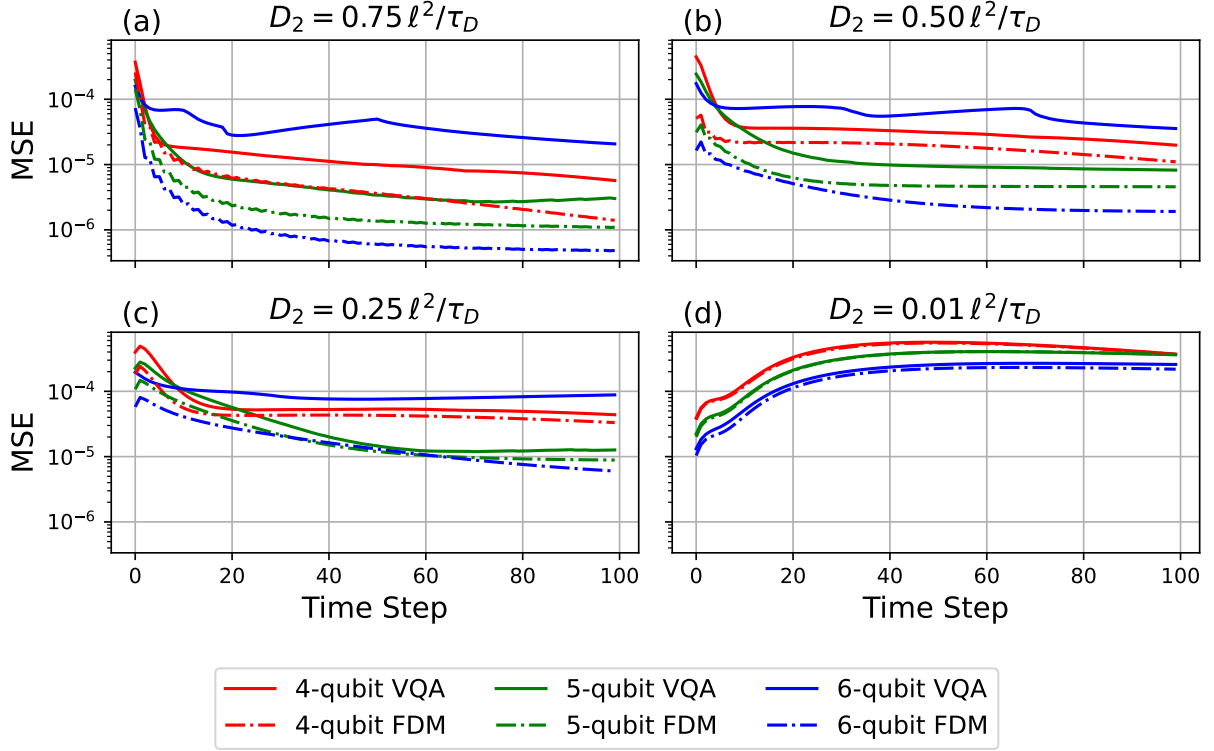


FIG. 8: Mean squared error (MSE) versus time step l of the FDM and VQA solutions relative to the analytical solution with $D_1 = 1 \ell^2 / \tau_D$ and $D_2 = 0.01, 0.25, 0.50, 0.75 \ell^2 / \tau_D$ obtained with 4-, 5- and 6-qubit statevector simulations.

initial conditions, compared to later times. Since the relaxation rate decreases as $D_2 \rightarrow 0$, the spatial charge profile $c(x, t)$ changes very slowly in time. Apart from that, the closer the discrete charge profiles c^l at consecutive time steps, the closer the corresponding variational parameters λ^l of the VQA ansatz. Therefore, when $D_2 = 0.01 \ell^2 / \tau_D$, the variational parameters change moderately, resulting in a relatively low number of iterations required by the optimization routine. Table I shows the computation time used in the BFGS algorithm in the aforementioned experiments. As is evident, the computation time increases with both the number of qubits and the diffusivity of the membrane.

Large computation times presented in Table II have a dependence on the number of qubits n , but this dependence is not straightforward. Increasing n leads to a dimension of the solution space growing as $N = 2^n$, which requires the ansatz circuit to encode solutions in higher-dimensional spaces. The simplest approach allowing actual solutions of the problem to be discovered by the ansatz circuit is to increase its depth thus improving its expressibility. However, as the ansatz circuit depth grows, the gradients of the VQA cost function vanish exponentially, requiring more computational resources to estimate the cost function accurately [45]. Consequently, the optimization process is dominated by statevector simulations as shown in Table II, as the increasingly flat cost

No. of qubits n	AEM diffusivity D_2	Time
4	0.01	0.18 h
	0.25	0.40 h
	0.50	0.41 h
	0.75	0.46 h
5	0.01	1.55 h
	0.25	3.88 h
	0.50	3.62 h
	0.75	4.52 h
6	0.01	25.44 h
	0.25	76.51 h
	0.50	76.02 h
	0.75	76.21 h

TABLE I: Comparison of computation time of the algorithm for different qubit numbers n and diffusivity constants D_2 . All ideal statevector simulations are done with the BFGS algorithm.

function forces the optimization algorithm to perform numerous evaluations to identify reliable search directions. Therefore, the actual bottleneck is not the classical optimization algorithm, but the ansatz circuit itself. Moreover, changing the optimization algorithm does not mitigate the problem, as the issue affects both gradient-free and gradient-based optimization algorithms [46].

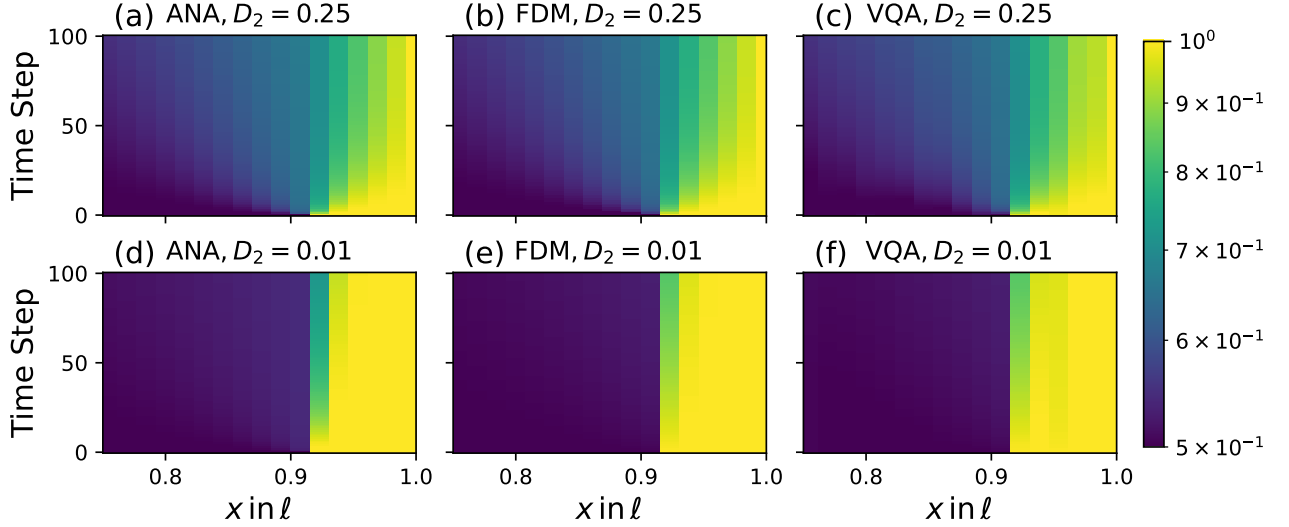


FIG. 9: Comparison between the time evolutions shown in panels (a)-(c) for $D_2 = 0.25 \ell^2/\tau_D$ and panels (d)-(f) for $D_2 = 0.01 \ell^2/\tau_D$. The number of interior grid points used in the simulations is $N = 64$. The x-axis is restricted to the range $x \in [0.75, 1] \ell$, since the concentration is nearly zero for $x < 0.75 \ell$.

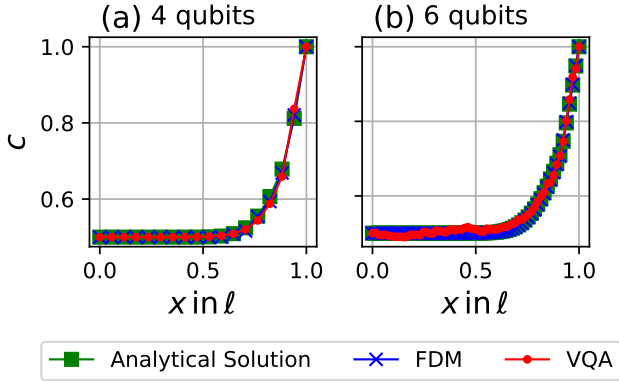


FIG. 10: Concentration profile for $D_2 = 0.5 \ell^2/\tau_D$ at $t = 8 \times 10^{-3} \tau_D$ for (a) 4 qubits and (b) 6 qubits.

No. of qubits n	BFGS	Statevector	Total
4	2 s	280 s	282 s
5	7 s	1953 s	1960 s
6	29 s	15913 s	15942 s

TABLE II: Comparison of computation times of different parts of the VQA algorithm for different qubit numbers n . The computation times for the statevector simulations and the calculations performed solely by the BFGS algorithm were measured separately. In all 4-, 5- and 6-qubit experiments the equation was solved for 10 time steps.

We also compared various optimization routines for $n = 4$ and $D_2 = 0.5 \ell^2/\tau_D$, namely, the BFGS algorithm, the Nelder-Mead (NM) algorithm, and the SBO algo-

rithm. For the SBO algorithm, we used both the FPS and HPS approaches and varied the number of sample points τ . In the HPS method, the empirical parameter γ was set to 1, effectively doubling the anticipated distance between variational parameters. Other parameters, such as ϵ_i , ϵ_{int} and ϵ_f were set to 0, $\ell^0/20$ and $\ell^0/2$ respectively. To ensure a fair comparison, all optimization algorithms employed the same number of function evaluations, n_{fev} . The results are presented in Fig. 12. The BFGS and NM algorithms achieved similar performance in terms of MSE, both yielding values on the order of 10^{-4} , with NM producing marginally higher errors. The SBO algorithm produced MSE values on the order of $10^{-1} \sim 10^{-2}$, which is worse than those achieved by BFGS and NM. With the FPS approach, the corresponding MSE does not improve when increasing the number of sample points. However, when using the HPS approach, increasing the number of sample points reduces the error to the order of 10^{-2} .

We also conducted 5-qubit statevector simulations using the aforementioned algorithms, wherein only the HPS approach was utilized for the SBO algorithm. In these tests, the BFGS algorithm demonstrated better performance in comparison to 4 qubits and convergent behavior in terms of MSE, whereas both the NM and SBO algorithms exhibited a stronger increasing MSE. As all algorithms were allocated with the same number of function evaluations, these results indicate that NM and SBO require more function evaluations to reach higher accuracy compared to BFGS. The analysis demonstrates again one weakness of the VQA methods, the choice and tuning of the classical optimization procedure for the non-convex minimum search of the cost function is task-specific.

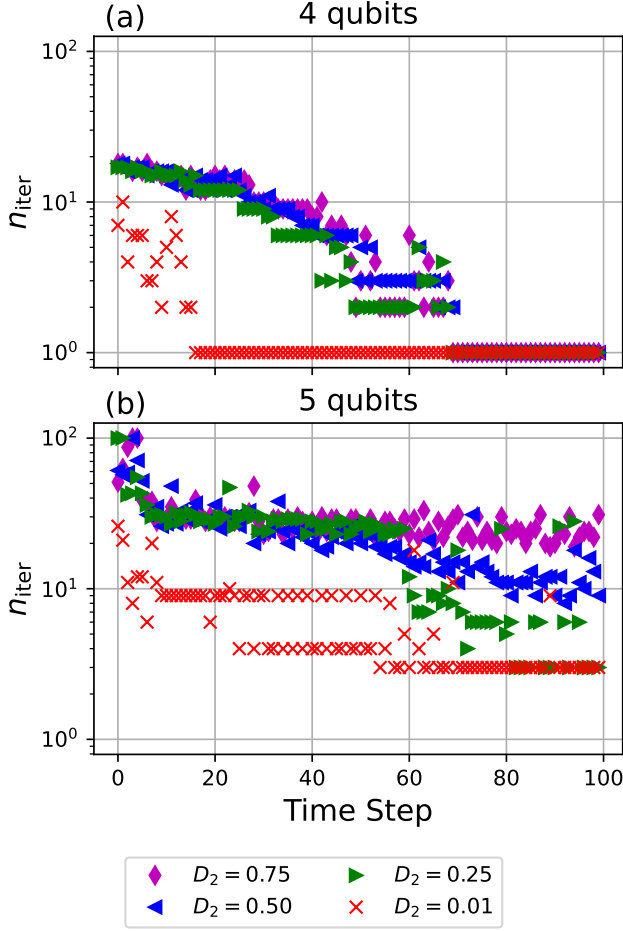


FIG. 11: Number of iterations of the BFGS optimization algorithm in the VQA for (a) 4 qubits and (b) 5 qubits.

V. CONCLUSION

The objective of the present work has been to investigate the diffusive ion transport problem across a multi-layered anion exchange membrane (AEM) and simulate it using a quantum algorithm. The ion transport problem is formulated as a time-dependent linear and one-dimensional diffusion problem with a space-dependent diffusion coefficient and inhomogeneous Dirichlet boundary conditions. Since the problem does not represent a unitary time evolution and is subject to non-periodic boundary conditions, it requires a specific quantum algorithm implementation with corresponding boundary treatment, similar to [27].

The quantum algorithm used for solving the diffusion problem is a variational quantum algorithm (VQA) based on the weak formulation framework. We have investigated its performance under ideal statevector simulations using $N = 16, 32, 64$ spatial grid points corresponding to 4, 5, and 6 data qubits, respectively. Moreover, we simultaneously varied the diffusivity of the anion exchange

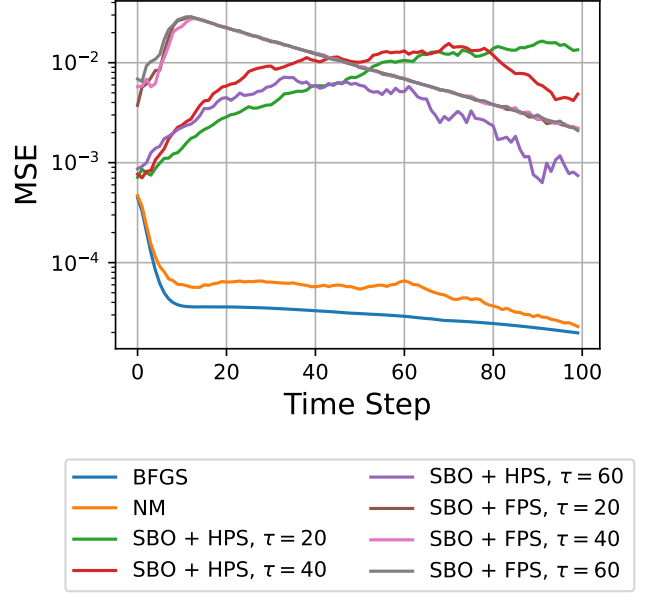


FIG. 12: Comparison of various classical optimization algorithms for the case with $D_2 = 0.5 \ell^2 / \tau_D$ using $N = 16$ (4 qubits) interior grid points.

membrane (AEM) from $D_2 = 0.01 \ell^2 / \tau_D$ to $0.75 \ell^2 / \tau_D$ while keeping $D_1 = 1 \ell^2 / \tau_D$ fixed. This varies the magnitude of the discontinuity inside the two-layer membrane. The algorithm's performance was measured using the mean squared error (MSE), which quantifies the deviation from the analytical solution, the latter of which we could derive for the present benchmark case. The obtained MSE of the VQA was then also compared with that of a conservative finite difference method (FDM).

The results obtained by ideal statevector simulations are a proof of concept that the VQA can solve the diffusion problem numerically. The accuracy of the time evolution in the VQA was bounded below by that of the FDM method, similar to the investigations in ref. [25]. By comparing the MSE of the VQA and the FDM, we were able to conclude that their performance depends not only on the number of grid points (number of qubits in the VQA) used to resolve the spatial coordinate, but also on the discontinuity of the diffusion constants of the layers of the AEM. More detailed, in the low diffusivity regime, the FDM performance deteriorated, and the VQA performance became almost identical to the FDM. The AEM diffusivity also impacted the computational effort of the optimization part of the VQA, meaning a low diffusivity regime results in faster convergence to the optimal solution, see again Table I. We compared three different classical optimization schemes to find the minimum of the cost function. The surrogate-based optimization scheme by Shaffer et al. [35], which we adapted to the present problem, did not lead to a better performance for the present application case in comparison to standard algorithms like Nelder-Mead or BFGS schemes.

BFGS gave the best results for our case.

Due to the cross-disciplinary nature of the problem considered in this work, the future research directions can be separated into two major categories, namely, (1) physical modeling of the multi-layered AEM and (2) further studies related to the VQA itself. To ensure the practical relevance, the multi-layered AEM model can be refined by, for instance, considering the AEM diffusivity dependence on the anion concentration field, modeling water concentration within the AEM [47] and/or accounting for the electric field distribution [48]. This, in turn, will transform the problem from a relatively simple diffusion equation into a system of coupled nonlinear partial differential equations, which will pose additional challenges to the quantum algorithm.

Concerning the VQA, the structure of the RPQC has a substantial impact on the high-dimensional parameter landscape of the non-convex optimization problem. The optimization is problem-specific, and thus, complexity estimates for the algorithm as a whole will remain difficult. Therefore, the RPQC has to be chosen according to the diffusion problem, and ideally, a problem-specific ansatz circuit can lead to drastic improvement towards optimization and necessary fidelity. Finally, noisy quantum

circuit and shot-based simulations have to be conducted, as they can reveal the actual performance of the quantum algorithm on real quantum computing devices. These efforts are underway and will be reported elsewhere.

ACKNOWLEDGEMENTS

The work of T.G. and P.P. is funded by the European Union (ERC, MesoComp, 101052786). Views and opinions expressed are, however, those of the authors only and do not necessarily reflect those of the European Union or the European Research Council. F.S. is supported by the Deutsche Forschungsgemeinschaft (DFG). The work benefited from helpful discussions with Sachin S. Bharadwaj, Sergio Bengoechea, Paul Over, and Katepalli R. Sreenivasan.

DATA AVAILABILITY

The Python scripts for processing the data in VQA algorithms will be made available once the manuscript is accepted for publication.

-
- [1] Z. Yan, J. L. Hitt, J. A. Turner, and T. E. Mallouk, Renewable electricity storage using electrolysis, *Proc. Natl. Acad. Sci. USA* **117**, 12558 (2020).
 - [2] M. El-Shafie, Hydrogen production by water electrolysis technologies: A review, *Results Engin.* **20**, 101426 (2025).
 - [3] H. I. Lee, M. Mehdi, S. K. Kim, H. S. Cho, M. J. Kim, W. C. Cho, Y. W. Rhee, and C. H. Kim, Advanced zircon-type porous separator for a high-rate alkaline electrolyser operating in a dynamic mode, *J. Membr. Sci.* **616**, 118541 (2020).
 - [4] M. Schalenbach, W. Lueke, and D. Stolten, Hydrogen diffusivity and electrolyte permeability of the zircon per separator for alkaline water electrolysis, *J. Electrochem. Soc.* **163**, F1480 (2016).
 - [5] J. Brauns, J. Schönebeck, M. R. Kraglund, D. Aili, J. Hnát, J. Žitka, W. Mues, J. O. Jensen, K. Bouzek, and T. Turek, Evaluation of diaphragms and membranes as separators for alkaline water electrolysis, *J. Electrochem. Soc.* **168**, 014510 (2021).
 - [6] E. Delp, R. Mishra, and E. Wagner, Evaluation of complex multi-physics phenomena at gas diffusion electrodes during high-pressure water electrolysis with aems, *Sci. Rep.* **15**, 24866 (2025).
 - [7] N. Du, C. Roy, R. Peach, M. Turnbull, S. Thiele, and C. Bock, Anion-exchange membrane water electrolyzers, *Chem. Rev.* **122**, 11830 (2022).
 - [8] D. Henkensmeier, W. C. Cho, P. Jannasch, J. Stojadinovic, Q. Li, D. Aili, and J. O. Jensen, Separators and membranes for advanced alkaline water electrolysis, *Chem. Rev.* **124**, 6393 (2024).
 - [9] Y. Sugawara, S. Sankar, S. Miyanishi, R. Illathvalappil, P. K. Gangadharan, H. Kuroki, G. M. Anilkumar, and T. Yamaguchi, Anion exchange membrane water electrolyzers: An overview, *J. Chem. Eng. Jpn.* **56**, 2210195 (2023).
 - [10] M. G. Marino, J. P. Melchior, A. Wohlfarth, and K. D. Kreuer, Hydroxide, halide and water transport in a model anion exchange membrane, *J. Membr. Sci.* **464**, 61 (2018).
 - [11] T. Zelovich, L. Vogt-Maranto, M. A. Hickner, S. J. Paddison, C. Bae, D. R. Dekel, and M. E. Tuckerman, Hydroxide ion diffusion in anion-exchange membranes at low hydration: Insights from ab initio molecular dynamics, *Chem. Mater.* **31**, 5778 (2019).
 - [12] C. Chen, Y.-L. S. Tse, G. E. Lindberg, C. Knight, and G. A. Voth, Hydroxide solvation and transport in anion exchange membranes, *J. Am. Chem. Soc.* **138**, 991 (2016).
 - [13] M. Al Otmi, P. Lin, W. Schertzer, C. M. Colina, R. Ramprasad, and J. Sampath, Investigating correlations in hydroxide ion transport in anion exchange membranes from atomistic molecular dynamics simulations, *ACS Appl. Polym. Mater.* **6**, 11270 (2024).
 - [14] A. J. Bard and L. R. Faulkner, *Electrochemical Methods – Fundamentals and Applications* (John Wiley & Sons, New York, 2001).
 - [15] M. Nielsen and I. Chuang, *Quantum Computation and Quantum Information: 10th Anniversary Edition* (Cambridge University Press, Cambridge, UK, 2010).
 - [16] J. Preskill, Quantum computing in the NISQ era and beyond, *Quantum* **2**, 79 (2018).
 - [17] S. S. Bharadwaj and K. R. Sreenivasan, Quantum computation of fluid dynamics, *Indian Academy of Sciences Conference Series* **3**, 77 (2020).

- [18] S. Succi, W. Itani, K. R. Sreenivasan, and R. Steijl, Quantum computing for fluids: Where do we stand?, *Europhys. Lett.* **144**, 10001 (2023).
- [19] F. Tennie, S. Laizet, S. Lloyd, and L. Magri, Quantum computing for nonlinear differential equations and turbulence, *Nat. Rev. Phys.* **7**, 1 (2025).
- [20] M. Cerezo, A. Arrasmith, R. Babbush, S. C. Benjamin, S. Endo, K. Fujii, J. R. McClean, K. Mitarai, X. Yuan, L. Cincio, and P. J. Coles, Variational quantum algorithms, *Nat. Rev. Phys.* **3**, 625 (2021).
- [21] R. Demirdjian, D. Gunlycke, C. A. Reynolds, J. D. Doyle, and S. Tafur, Variational quantum solutions to the advection–diffusion equation for applications in fluid dynamics, *Quant. Inf. Process.* **21**, 322 (2020).
- [22] F. Y. Leong, W.-B. Ewe, and D. E. Koh, Variational quantum evolution equation solver, *Sci. Rep.* **12**, 10817 (2022).
- [23] F. Y. Leong, D. E. Koh, W.-B. Ewe, and J. F. Kong, Variational quantum simulation of partial differential equations: Applications in colloidal transport, *Int. J. Num. Meth. Heat Fluid Flow* **33**, 3669 (2023).
- [24] D. Jaksch, P. Givi, A. J. Daley, and T. Rung, Variational quantum algorithms for computational fluid dynamics, *AIAA J.* **61**, 1885 (2023).
- [25] J. Ingelmann, S. Bharadwaj, P. Pfeffer, K. Sreenivasan, and J. Schumacher, Two quantum algorithms for solving the one-dimensional advection-diffusion equation, *Comput. Fluids* **281**, 106369 (2024).
- [26] S. Bengoechea, P. Over, D. Jaksch, and T. Rung, Toward variational quantum algorithms for generalized linear and nonlinear transport phenomena, *AIAA J.*, 1 (2025).
- [27] P. Over, S. Bengoechea, T. Rung, F. Clerici, L. Scandurra, E. de Villiers, and D. Jaksch, Boundary treatment for variational quantum simulations of partial differential equations on quantum computers, *Comput. Fluids* **288**, 106508 (2025).
- [28] N. M. Guseynov, A. A. Zhukov, W. V. Pogosov, and A. V. Lebedev, Depth analysis of variational quantum algorithms for the heat equation, *Phys. Rev. A* **107**, 052422 (2023).
- [29] Y. Y. Liu, Z. Chen, C. Shu, S. C. Chew, B. C. Khoo, X. Zhao, and Y. D. Cui, Application of a variational hybrid quantum-classical algorithm to heat conduction equation and analysis of time complexity, *Phys. Fluids* **34**, 117121 (2023).
- [30] M. Lubasch, J. Joo, P. Moinier, M. Kiffner, and D. Jaksch, Variational quantum algorithms for nonlinear problems, *Phys. Rev. A* **101**, 010301(R) (2020).
- [31] N. Köcher, H. Rose, S. S. Bharadwaj, J. Schumacher, and S. Schumacher, Numerical solution of nonlinear Schrödinger equation by a hybrid pseudospectral-variational quantum algorithm, *Sci. Rep.* **15**, 23478 (2025).
- [32] A. J. Pool, A. D. Somoza, M. Lubasch, and B. Horstmann, Solving partial differential equations using a quantum computer, *2022 IEEE International Conference on Quantum Computing and Engineering*, 864 (2022).
- [33] A. J. Pool, A. D. Somoza, C. McKeever, M. Lubasch, and B. Horstmann, Nonlinear dynamics as a ground-state solution on quantum computers, *Phys. Rev. Res.* **6**, 033257 (2024).
- [34] P. Pfeffer, P. Brearley, S. Laizet, and J. Schumacher, Spectral quantum algorithm for passive scalar transport in shear flows, *Sci. Rep.* **15**, 41172 (2025).
- [35] R. Shaffer, L. Kocia, and M. Sarovar, Surrogate-based optimization for variational quantum algorithms, *Phys. Rev. A* **107**, 032415 (2023).
- [36] Z. Holmes, K. Sharma, M. Cerezo, and P. J. Coles, Connecting Ansatz Expressibility to Gradient Magnitudes and Barren Plateaus, *PRX Quantum* **3**, 010313 (2022).
- [37] S. Sim, P. D. Johnson, and A. Aspuru-Guzik, Expressibility and entangling capability of parameterized quantum circuits for hybrid quantum-classical algorithms, *Adv. Quantum Technol.* **2**, 1900070 (2019).
- [38] P. Bressloff, Accumulation time of diffusion in a two-dimensional singularly perturbed domain, *Proc. R. Soc. A* **478**, 20210847 (2022).
- [39] A. G. Neelan, F. S. Don Bosco, N. S. Jarugumalli, and S. B. Vedarethinam, Physics-informed neural networks: Bridging the divide between conservative and non-conservative equations, preprint arXiv:2506.22413 <https://doi.org/10.48550/arXiv.2506.22413> (2025).
- [40] J. Lee, *Stability of finite difference schemes on the diffusion equation with discontinuous coefficients*, Master's thesis, Department of Mathematics, Massachusetts Institute of Technology (2017).
- [41] B. Zindorf and S. Bose, Efficient implementation of multi-controlled quantum gates, *Phys. Rev. Applied* **24**, 044030 (2025).
- [42] A. Javadi-Abhari, M. Treinish, K. Krsulich, C. J. Wood, J. Lishman, J. Gacon, S. Martiel, P. D. Nation, L. S. Bishop, A. W. Cross, B. R. Johnson, and J. M. Gambetta, Quantum computing with Qiskit, preprint arXiv:2405.08810v3 <https://doi.org/10.48550/arXiv.2405.08810> (2024).
- [43] K. Życzkowski and H.-J. Sommers, Average fidelity between random quantum states, *Phys. Rev. A* **71**, 032313 (2005).
- [44] J. A. Nelder and R. Mead, A simplex method for function minimization, *Comput. J.* **7**, 308 (1965).
- [45] S. Liu, S.-X. Zhang, S.-K. Jian, and H. Yao, Training variational quantum algorithms with random gate activation, *Phys. Rev. Res.* **5**, L032040 (2023).
- [46] A. Arrasmith, M. Cerezo, P. Czarnik, L. Cincio, and P. J. Coles, Effect of barren plateaus on gradient-free optimization, *Quantum* **5**, 558 (2021).
- [47] K. Yassin, I. G. Rasin, S. Brandon, and D. R. Dekel, Quantifying the critical effect of water diffusivity in anion exchange membranes for fuel cell applications, *J. Membr. Sci.* **608**, 118206 (2020).
- [48] D. R. Dekel, I. G. Rasin, M. Page, and S. Brandon, Steady state and transient simulation of anion exchange membrane fuel cells, *J. Power Sources* **375**, 191–204 (2018).